Validation of OMI, GOME-2A, and GOME-2B tropospheric NO_2, SO_2, and HCHO products using MAX-DOAS observations from 2011 to 2014 in Wuxi, China: investigation of the effects of priori profiles and aerosols on the satellite products

Yang Wang[1], Steffen Beirle[1], Johannes Lampel[1,2], Mariliza Koukouli[3], Isabelle De Smedt[4], Nicolas Theys[4], Ang Li[5], Dexia Wu[5], Pinhua Xie[5,6,7], Cheng Liu[8,6,5], Michel Van Roozendael[4], Trissevgeni Stavrakou[4], Jean-François Müller[4], and Thomas Wagner[1]

[1] Max Planck Institute for Chemistry, Mainz, Germany
[2] Institute of Environmental Physics, University of Heidelberg, Heidelberg, Germany
[3] Laboratory of Atmospheric Physics, Aristotle University of Thessaloniki, Thessaloniki, Greece
[4] Belgian Institute for Space Aeronomy (BIRA-IASB), Brussels, Belgium
[5] Anhui Institute of Optics and Fine Mechanics, Chinese Academy of Sciences, Hefei, China
[6] CAS Center for Excellence in Urban Atmospheric Environment, Institute of Urban Environment, Chinese Academy of Sciences, Xiamen, China
[7] School of Environmental Science and Optoeclectronic Technology, University of Science and Technology of China, Hefei, China
[8] School of Earth and Space Sciences, University of Science and Technology of China, Hefei, China

Correspondence to: Yang Wang (y.wang@mpic.de), Ang Li (Angli@aiofm.ac.cn), Cheng Liu (chliu81@ustc.edu.cn)

Abstract.

Tropospheric vertical column densities (VCDs) of NO_2, SO_2, and HCHO derived from the Ozone Monitoring Instrument (OMI) on AURA and the Global Ozone Monitoring Experiment 2 aboard METOP-A (GOME-2A) and METOP-B (GOME-2B) are widely used to characterize the global distributions, trends, dominating sources of these trace gases. They are also useful for the comparison with chemical transport models (CTM). We use tropospheric VCDs and vertical profiles of NO_2, SO_2 and HCHO derived from MAX-DOAS measurements from 2011 to 2014 in Wuxi, China, to validate the corresponding products (daily and bimonthly averaged data) derived from OMI and GOME-2A/B by different scientific teams. Prior to the comparison, the spatial and temporal coincidence criteria for MAX-DOAS and satellite data are determined by a sensitivity study using different spatial and temporal averaging conditions. Cloud effects on both MAX-DOAS and satellite observations are also investigated. Our results indicate that the discrepancies between satellite and MAX-DOAS results increase with increasing effective cloud fraction and are dominated by the effects of clouds on the satellite products. In comparison with MAX-DOAS, we found a systematic underestimation of all SO_2 (40% to 57%) and HCHO products (about 20%), and an overestimation of the GOME-2A/B NO_2 products (about 30%), but good consistency with the DOMINO version 2 NO_2 product. To better understand the reasons for these differences, we evaluated the a-priori profile shapes used in the OMI retrievals (derived from CTM) by comparison with those derived from the MAX-DOAS observations. Significant differences are found for the SO_2 and HCHO profile shapes derived from the IMAGES model, whereas on

average good agreement is found for the NO_2 profile shapes derived from the TM4 model. We also applied the MAX-DOAS profile shapes to the satellite retrievals and found that these modified satellite VCDs agree better with the MAX-DOAS VCDs than the VCDs from the original data sets by up to 10%, 47% and 35% for NO_2, SO_2 and HCHO, respectively. Furthermore, we investigated the effect of aerosols on the satellite retrievals. For OMI observations of NO_2, a systematic underestimation is found for large AOD, which is mainly attributed to effect of the aerosols on the cloud retrieval and the subsequent application of a cloud correction scheme (implicit aerosol correction). In contrast, the effect of aerosols on the clear sky AMF (explicit aerosol correction) has a smaller effect. For SO_2 and HCHO observations selected in the same way, no clear aerosol effect is found, probably because for the considered data sets no cloud correction is applied (and also because of the larger scatter). From our findings we conclude that for satellite observations with cloud top pressure (CTP) > 900hPa and effective cloud fraction (eCF) < 10% the application of a clear sky AMF might be a good option if accurate aerosol information is not available. Another finding of our study is that the ratio of morning to afternoon NO_2 VCDs can be considerably overestimated if results from different sensors and/or retrievals (e.g. OMI and GOME-2) are used, whereas less deviations for HCHO and SO_2 VCDs are found .

1 Introduction

Nitrogen oxides ($NO_x \equiv NO_2 + NO$), sulphur dioxide (SO_2), and formaldehyde (HCHO) play critical roles in tropospheric chemistry through various gas phase and multi-phase chemical reactions (Seinfeld and Pandis, 1998). In an urban and industrialized region, anthropogenic emissions from traffic, domestic heating, factories, power plants and biomass burning significantly elevate the concentrations of these (and other) trace gases (TGs) in the boundary layer (Environmental Protection Agency, 1998; Seinfeld and Pandis, 1998). There is strong evidence that aerosol particles formed through photochemistry of NO_x, SO_2, and VOCs significantly contribute to haze pollution events occurring frequently around megacities and urban agglomerations in China, like the Jing–Jin–Ji region and the Yangtze River Delta region (Crippa et al., 2014; Huang et al., 2014; Jiang et al., 2015; Fu et al., 2014). The aerosols also impact the local radiative forcing through direct (e.g. McCormic and Ludwig, 1967) and indirect effects (Lohmann and Feichter, 2005). Understanding global and regional distributions and temporal variations of the TGs, and further identifying and quantifying their dominant sources can provide a firm basis for a better understanding of the formation mechanisms of haze pollution and for the development of mitigation strategies.

Since 1995 a series of sun-synchronous satellites, such as ERS-2, ENVISAT, AURA, METOP-A and METOP-B, was launched carrying UV/vis/NIR spectrometers with moderate spectral resolution, which allowed scientists to determine global distributions of several important tropospheric trace gases including NO_2, HCHO and SO_2 for the first time. The first instrument was the Global Ozone Monitoring Experiment (GOME) (Burrows et al., 1999), followed by the SCanning Imaging Absorption spectroMeter for Atmospheric CHartographY (SCIAMACHY) (e.g. Bovensmann et al., 1999), the Ozone Monitoring Instrument (OMI) (Levelt et al., 2006a, b), and the GOME-2A and GOME-2B instruments (Callies et al.,

2000; Munro et al., 2006, 2016). The OMI and GOME-2A/B instruments are still in operation. A large number of studies developed retrieval algorithms for these instruments to acquire the tropospheric vertical column densities (VCD) of NO_2 (e.g. Boersma et al., 2004, 2007 and 2011; Richter et al., 2005; Beirle et al., 2010 and Valks et al., 2011), SO_2 (e.g. Krueger et al., 1995; Eisinger and Burrows, 1998; Carn et al., 2004; Krotkov et al., 2006; Richter et al., 2006 and 2009; Yang et al., 2007; Lee et al., 2009; Nowlan et al., 2011; Rix et al., 2012; Li et al., 2013; Theys et al., 2015), and HCHO (Chance et al., 2000; Palmer et al., 2001; Wittrock et al., 2006a; De Smedt et al., 2008, 2012 and 2015; Kurosu, 2008; Millet et al., 2008; Hewson et al., 2013; González Abad et al., 2015). In this validation study we include several products, which are published recently and are widely used: for NO_2 the near-real-time OMI DOMINO v2.0 (Boersma et al., 2007 and 2011) and the GOME-2A/B TM4NO2A (Boersma et al., 2004); for SO_2 the operational OMSO2 OMI product (Li et al., 2013) published by National Aeronautics and Space Administration (NASA), the O3M-SAF operational GOME-2A product published by the German Aerospace Centre (DLR) (Rix et al., 2012 and Hassinen et al., 2016), and the OMI and GOME-2A/B products developed by BIRA (Theys et al., 2015); for HCHO the OMI and GOME-2A/B products developed by BIRA (De Smedt et al., 2008, 2012 and 2015). Many users already benefit from these products for several applications, e.g. detection and quantification of emissions, identification of transport processes and chemical transformations, and for the comparison with model simulations (e.g. Beirle et al., 2003 and 2011; Martin et al., 2003; Richter et al., 2005; van der A et al., 2008; Herron-Thorpe et al., 2010; Gonzi et al., 2011; Barkley et al., 2012; Koukouli et al., 2016).

Although several studies have paid efforts to improve satellite retrievals, still significant differences compared to ground based measurements were reported by several validation studies, e.g. a systematic underestimation of the tropospheric VCDs of NO_2, SO_2 and HCHO was obtained for OMI by > 30% in or near Beijing, China (Ma et al., 2013; Theys, et al., 2015 and De Smedt et al., 2015; Jin, et al., 2016). The satellite retrieval errors are mainly attributed to the slant column retrievals (spectral analysis), the stratospheric correction (for NO_2) and the tropospheric air mass factor (AMF) calculations. The AMF uncertainties are related to several factors, such as the surface albedo, the cloud and aerosol properties, methodological assumptions on how clouds and aerosols should be accounted for (Lin et al., 2015), the a-priori profile shape (also referred to as the shape factor (SF) in the following) as well as interpolation errors of the discrete look-up table entries (Lin et al., 2014). Thus validation studies for satellite products using independent ground-based measurements are essential to quantify uncertainties, identify dominant error sources and to further improve the satellite retrieval algorithms.

Since about 15 years ago, the Multi Axis - Differential Optical Absorption Spectroscopy (MAX-DOAS) technique (Hönninger and Platt, 2002; Bobrowski et al., 2003; Van Roozendael et al., 2003; Hönninger et al., 2004; Wagner et al., 2004 and Wittrock et al., 2004), is applied to retrieve tropospheric vertical profiles of TGs and aerosols from spectra of scattered UV/Visible sunlight measured at different elevation angles (e.g. Frieß et al., 2006, 2011 and 2016; Wittrock et al., 2006b; Irie et al., 2008 and 2011; Clemer et al., 2010; Li et al., 2010 and 2012; Vlemmix et al., 2010, 2011 and 2015b; Wagner et al., 2011; Yilmaz, 2012; Hartl and Wenig, 2013 and Wang et al., 2013a and b). MAX-DOAS observations provide valuable information that can be applied for a quantification of air pollutants (e.g. Li et al., 2012; Hendrick et al., 2014; Wang et al., 2014a; Wang et al., 2016), a validation of tropospheric satellite products (e.g. Irie et al., 2012 and 2016;

Ma et al., 2013; Kanaya et al., 2014; Theys, et al., 2015 and De Smedt et al., 2015; Jin et al., 2016), and an evaluation of chemical transport model (CTM) simulations (e.g. Vlemmix et al., 2015a). The tropospheric vertical profiles are also valuable for the evaluation of SFs used in the satellite AMF calculations. Here it is important to note that many studies already investigated the effect of the a-priori SFs on the satellite retrievals (i.e. Boersma et al., 2004; Hains et al., 2010; Heckel et al., 2011) and demonstrated that the SF effect on the tropospheric AMFs can dominate the systematic errors of tropospheric satellite products, especially in highly polluted (urban and industrial) regions (Boersma et al., 2011, Theys et al., 2015 and De Smedt et al., 2015). Nevertheless, because profile measurements are rare, the SF effect is still not well understood in many regions. In this study the SF effect on the tropospheric AMF will be investigated using the vertical profiles of the TGs derived from the MAX-DOAS observations in Wuxi, China from 2011 to 2014 (Wang et al., 2016).

Wuxi is located about 130 km north-west of Shanghai belonging to the most industrialized part of the Yangtze River delta (YRD) region. YRD including Shanghai City and four nearby provinces is the largest economic region in China. It is heavyly industrialized and can be considered as the largest metropolitan area in Asia with a population of about 150 millions. Several studies already used satellite products of the pollutants to quantify the corresponding emissions (Ding et al., 2015; Han et al., 2015; Bauwens et al., 2016) in this region. However validation studies for the satellite products in this region are still sparse. Chen et al. (2009), Irie et al. (2012), Kanaya et al. (2014), and Chan et al. (2015) validated the satellite NO_2 tropospheric VCD products using MAX-DOAS (or zenith-sky DOAS) measurements in Rudong, Hefei, and Shanghai. So far there are no validation reports for SO_2 and HCHO products in the YRD region. However several validation studies have been carried out in other regions of China (e.g. Theys et al., 2015; De Smedt et al., 2015; Jin et al., 2016).

In this study we validate daily (2 hours around the satellite overpass time) and bi-monthly averages of the tropospheric VCDs of NO_2, SO_2, and HCHO derived from OMI and GOME-2 using the MAX-DOAS observations in Wuxi, and we discuss in particular the influence of the coincidence criteria on the comparison results. Previous studies (Ma et al., 2013 and Jin et al., 2016) already presented comparison studies and discussed several aspects limiting the consistency between satellite and MAX-DOAS observations. Concerning the impact of clouds on both MAX-DOAS and satellite retrievals, we separately evaluate the cloud effects on both satellite and MAX-DOAS observations. Also the weekend effect and ratios of morning and afternoon values (representing diurnal variations) acquired by combining GOME-2 and OMI observations are evaluated by comparison with similar ratios derived from the corresponding MAX-DOAS results..

For most of the satellite products aerosol information is not considered in radiative transfer models (RTM) used for the AMF calculations (one exception is the OMI NO_2 product (POMINO) provided by the Peking University over China (Lin et. al., 2014)), but recently such aerosol effects have drawn more and more attention. Shaiganfar et al. (2011), Ma et al. (2013), and Kanaya et al. (2014) found negative biases of the OMI tropospheric NO_2 VCDs between 26 and 50 % over areas with high aerosol pollution through the validation by MAX-DOAS observations. But aerosol effects on the satellite retrievals are still not well understood. The aerosols effects can be generally separated into two contributions: a) the effect of aerosols on the satellite AMF compared to AMFs for a pure Rayleight atmosphere (explicit aerosol correction), and b) the effect of aerosols on the retrieval of cloud products (often referred to as "implicit aerosol correction", Boersma et al., 2011; Castellanos et al.,

2015; Chimot et al., 2016). These two contributions of aerosols on the satellite retrievals are discussed in this study based on the aerosol and TG profiles derived from the MAX-DOAS observations in Wuxi and by comparing the satellite TG VCDs to the corresponding results from the MAX-DOAS observations.

The paper is organized as follows: in section 2 we describe the MAX-DOAS observations in Wuxi and the satellite products involved in this study. In section 3 we compare the NO_2, SO_2 and HCHO VCDs derived from MAX-DOAS with those from the satellite instruments. We investigate in particular the effects of clouds, SFs, and aerosols on the satellite retrievals. In section 4 the conclusions are given.

2 MAX-DOAS measurements and satellite data sets

2.1 MAX-DOAS instrument and data analysis

A MAX-DOAS instrument developed by the Anhui Institute of Optics and Fine Mechanics (AIOFM) (Wang et al., 2015 and 2016) is located on the roof of a 11-story building in Wuxi City (Fig. 1 a), China (31.57 °N, 120.31 °E, 50 m a.s.l.) and operated by the Wuxi CAS Photonics Co. Ltd from May 2011 to Dec 2014. Wuxi City is located in the YRD region which is typically affected by high loads of NO_2, SO_2 and HCHO (Fig. 1 b, c, d). The DOAS method (Platt and Stutz, 2008) and the PriAM profile inversion algorithm (Wang et al., 2013a/b and 2016) are applied to derive the vertical profiles of aerosol extinction (AEs) and volume mixing ratios (VMRs) of NO_2, SO_2 and HCHO from scattered UV/visible sunlight recorded by the MAX-DOAS instrument at five elevation angles (5 °, 10 °, 20 °, 30 ° and 90 °). The telescope of the instrument is pointed to the north. The data analysis and the results derived from the MAX-DOAS measurements are already described in our previous study (Wang et al., 2016). In that study we compared the MAX-DOAS results with collocated independent techniques including an AERONET sun photometer, a visibility meter, and a long path DOAS. The comparisons were done for different cloud conditions as derived from a cloud classification scheme based on the MAX-DOAS observations (Wagner et al., 2014 and Wang et al., 2015). One important conclusion of that study was that meaningful trace gas profiles can be retrieved not only for clear skies, but also for most cloudy conditions (except for heavy fog or haze and optically thick clouds). Thus in this study we use all MAX-DOAS trace gas profiles obtained for these sky conditions (Wang et al., 2016). Here it is important to note that differently from previous studies (e.g. Ma et al., 2013; Jin et al., 2016), we derive the tropospheric VCDs of the TGs by an integration of the vertical profiles, but not by the so-called geometric approximation (e.g. Brinksma et al., 2008). Our previous study (Wang et al., 2016) demonstrated that the tropospheric trace gas VCDs from the full profile inversion are in general more accurate than those from the geometric approximation. The discrepancy of the VCDs derived by both methods is systematic and can be mainly attributed to the errors of the geometric approximation, for which the errors can be up to 30% depending on the observation geometry, and the properties of aerosols and TGs.

2.2 NO_2, SO_2 and HCHO products derived from OMI

The OMI instrument (Levelt et al., 2006a, b) aboard the sun-synchronous EOS Aura satellite was launched in July 2004. It achieves daily global coverage with a spatial resolution of 24×13 km^2 in nadir and about 150×13 km^2 at the swath edges (Levelt et al., 2006b). The overpass time is around 13:30 LT. In this study, we validate the operational level 2 (Boersma et al., 2007 and 2011) tropospheric NO_2 VCD (DOMINO version 2) obtained from the TEMIS website (http://www.temis.nl). The NO_2 SCDs are retrieved in the 405–465 nm spectral window using a DOAS algorithm and are converted to NO_2 tropospheric VCDs using tropospheric AMFs from a look-up table, which is generated using the DAK radiative transfer model (RTM) (Stammes, 1994), after the stratospheric column was subtracted. SFs of NO_2 for the AMF calculations are obtained from the TM4 CTM (Williams et al., 2009) for individual measurements and can be downloaded from the TEMIS website. TM4 assimilations run at a resolution of 2° ×3° (lat × lon) and 35 vertical levels up to 0.38 hPa and are spatially interpolated to the OMI pixel center (Boersma et al., 2007 and 2011; Dirksen et al., 2011). The effective cloud fraction (eCF) (Stammes et al., 2008; Wang et al., 2008) and cloud top pressure (CTP) (Acarreta et al., 2004) are obtained from the OMCLDO2 cloud product based on the O_4 absorption band at 477 nm assuming a Lambertian cloud with an albedo of 0.8. The retrieval algorithm for DOMINO v2 forms the basis of NO_2 retrievals for the upcoming TROPOspheric Monitoring Instrument (TROPOMI) aboard the Sentinel-5 Precursor mission (Veefkind et al., 2012).

Two data sets of tropospheric SO_2 VCDs derived from OMI observations are validated in this study. One is the operational level 2 OMSO2 planetary boundary layer (PBL) SO_2 data set (assuming SO_2 mostly in the PBL) provided via the NASA website (http://avdc.gsfc.nasa.gov). In the following this product is simply referred to as "OMI NASA". For the PBL SO_2 product, the VCD is derived from the measured radiances of the OMI instrument between 310.5 and 340 nm using a principal component analysis (PCA) algorithm (Li et al., 2013). A fixed surface albedo (0.05), surface pressure (1013.25 hPa), solar zenith angle (30°) and viewing zenith angle (0°) as well as a fixed climatological SO_2 profile over the summertime eastern U.S. are assumed in the PCA retrieval (Krotkov et al., 2008). The second product is derived by a new OMI SO_2 retrieval algorithm developed by BIRA (Theys et al., 2015). In the following this product is simply referred to as "OMI BIRA". It forms the basis of the algorithm for the operational level-2 SO_2 product to be derived from the upcoming TROPOMI instrument. SO_2 SCDs are first retrieved in a window between 312 –326 nm using the DOAS technique and then a background correction for possible biases is applied. The SO_2 SCDs are converted to VCDs using AMFs from a look-up table, which is generated using the LInearized Discrete Ordinate Radiative Transfer (LIDORT) version 3.3 RTM (Spurr et al., 2001 and 2008). SFs for SO_2 are obtained from the IMAGES CTM (Müller and Brasseur, 1995) for individual measurements at a horizontal resolution of 2° × 2.5° and at 40 vertical unevenly distributed levels extending from the surface to the lower stratosphere (44 hPa) (Stavrakou et al., 2013 and 2015). Like for the OMSO2 data set the cloud information is obtained from the OMCLDO2 cloud product.

The HCHO data set validated in this study is the OMI HCHO tropospheric VCD level 2 data retrieved by a DOAS algorithm v14 developed at BIRA-IASB (De Smedt et al., 2015). This algorithm will also be applied to the upcoming TROPOMI

instrument. HCHO SCDs are retrieved in the spectral window between 328.5–346 nm using the DOAS technique. After applying a background correction, HCHO SCDs are converted to tropospheric VCDs using AMFs from a look-up table generated by LIDORT with HCHO SFs obtained from the IMAGES CTM for individual measurements (Stavrakou et al., 2015). Also for this product the cloud information is obtained from the OMCLDO2 cloud product.

Here one important aspect should be noted: different AMF strategies are used in the DOMINO v2 NO_2 product and the BIRA SO_2 and HCHO products for eCF < 10%. For the NO_2 product the eCF and CTP are explicitly considered in the AMF simulations while for the SO_2 and HCHO products the clear sky AMFs are applied. These differences will be especially important for measurements in the presence of high aerosol loads (see section 3.5). For eCF>10%, a cloud correction based on the independent pixel approximation (IPA) (Cahalan et al., 1994) is applied for the three TG retrievals. It should also be noted that observations of the outermost pixels (i.e. pixel numbers 1–5 and 56–60) and pixels affected by the so called "row anomaly" (see http://www.temis.nl/docs/omiwarning.html) were removed before the comparisons.

2.3 NO_2, SO_2 and HCHO products derived from GOME-2

The GOME-2A and B instruments (Callies et al., 2000; Munro et al., 2006, 2016) are aboard the sun-synchronous Meteorological Operational Satellite platforms MetOp-A and MetOp-B, respectively. MetOp-A (launched on 19 October 2006) and MetOp-B (launched on 17 September 2012) operate in parallel with the same equator crossing time of 09:30 LT. Before 15 July 2013 GOME-2A had a swath width of 1920km, corresponding to a ground pixel size of 80 km×40 km and a global coverage within 1.5 days. Since 15 July 2013, the GOME-2A swath width was changed to 960 km with a ground pixel size of 40 km×40 km. The GOME-2A settings before 2013 are also applied to GOME-2B.

In this study, we validate the operational level 2 tropospheric NO_2 VCDs derived from the TM4NO2A version 2.3 product (Boersma et al., 2004) for GOME-2A and B obtained from the TEMIS website. The NO_2 SCDs are retrieved in the 425-450 nm spectral window by the BIRA team with QDOAS (http://uv-vis.aeronomie.be/software/QDOAS/). The tropospheric NO_2 VCDs are obtained from the SCDs using the similar data assimilation procedures as for the DOMINO v2 product. However, for the GOME-2 products the eCF and CTP are retrieved by the improved Fast Retrieval Scheme for Clouds from the Oxygen A-band algorithm (FRESCO+) based on the measurements of the oxygen A-band around 760 nm (Wang et al., 2008) again assuming a Lambertian cloud.

Two SO_2 products derived from GOME-2A observations are included in the study. The first one is the operational level 2 O3M-SAF SO_2 product derived from GOME-2A observations (Rix et al., 2012 and Hassinen et al., 2016). In the following the product is simply referred to as "GOME-2A DLR". This product is provided via the EUMETSAT product navigator (http://navigator.eumetsat.int) or the DLR EOWEB system (http://eoweb.dlr.de). The SO_2 SCDs are retrieved using the DOAS technique in the wavelength range between 315 and 326 nm. For the conversion of SCDs to VCDs, the AMFs are acquired from a look-up table generated using LIDORT 3.3. For the AMF computation, three types of SFs are assumed as Gaussian distributions with a FWHM of 1.5km around three central heights of 2.5km, 6km and 15km. Because for the SO_2

concentrations at Wuxi mostly anthropogenic pollutions is relevant, only the SO_2 product corresponding to the central height of 2.5 km is included in the validation study. The cloud information is obtained from GOME-2 measurements by the OCRA and ROCINN algorithms (Loyola et al., 2007) based on oxygen A-band observations at around 760 nm. The second product is provided by BIRA using the same retrieval algorithm as for the OMI BIRA SO_2 product, referred to as "GOME-2A BIRA". The same algorithm is also used to acquire the SO_2 data from GOME-2B observations. The product is referred to as "GOME-2B BIRA" in the following. The cloud properties used in the two products are derived from GOME-2A/B observations using the FRESCO+ algorithm.

The HCHO tropospheric VCD level 2 products derived from GOME-2A and B observations (De Smedt et al., 2012 and 2015) are validated in this study. The same retrieval approach as for the OMI BIRA HCHO product is applied, but the cloud properties are derived from GOME-2A/B observations using the FRESCO+ algorithm.

3 Validation of the satellite data sets

In this section the daily and bi-monthly averaged NO_2, SO_2, and HCHO VCDs from OMI and GOME-2 are validated by comparisons with the tropospheric VCDs derived from the MAX-DOAS observations. Here it needs to be clarified that the daily and bi-monthly satellite data are the averaged values of all satellite pixels located in the coincidence area around the measurement site (see below). The MAX-DOAS data are the averaged values for all measurements within 2 hours around the satellite overpass time. Also the diurnal and weekly cycles from the satellite observations are compared with those from the corresponding MAX-DOAS observations. Finally the influence of the SF and the effects of aerosols on the OMI products are discussed. The SFs from the CTM used for the OMI AMF calculations are compared to the SFs derived from MAX-DOAS.

Averaging of individual satellite and/or MAX-DOAS observations can be advantageous for several reasons. First, especially for observations with rather large statistical uncertainties (in particular for satellite observations of SO_2 and HCHO), the merging of several observations can substantially reduces these uncertainties. Second, the effect of spatial gradients across satellite pixels can be partly accounted for by averaging MAX-DOAS measurements over a period around the satellite overpass time. However, for the averaging of satellite and MAX-DOAS data reasonable selection criteria need to be determined, which can be different for the different TGs and satellite sensors. The effects of the selection criteria, in particular the time period used for the MAX-DOAS measurements and the distance of the selected satellite observations from the measurement site are evaluated and discussed in detail in section S1 in the supplement. One general finding is that the effect of the chosen time period is negligible compared to the effect of the chosen distance. Therefore it is reasonable to arbitrarily use 2 hours around the satellite overpass time, namely 12:30 LT to 14:30 LT for the comparisons with OMI and from 08:30 LT to 10:30 LT for the comparisons with GOME-2A/B. The distances around the measurement site, for which satellite observations are averaged are chosen differently for the different satellite products based on the sensitivity studies shown in section S1 in the supplement. In the following comparisons, the OMI NO_2 and SO_2 (HCHO) data are selected for

satellite pixels with distances <20km (<50km) from the Wuxi station. The GOME-2A/B data of the three species are selected for distances < 50km. It should be noted that these findings are derived for a polluted site in China. For other locations and conditions, different coincidence criteria might be best suited.

3.1 Daily comparisons

The daily averaged satellite data for measurements within the chosen distances are compared with the daily averaged MAX-DOAS data within 2 hours around the satellite overpass time. To characterize the cloud effect on the comparisons, the comparisons are performed for different eCF bins of 0-10%, 10-20%, 20-30%, 30-40%, 40-50%, and 50-100% for NO_2 and SO_2, and for eCF bins of 0-10%, 10-30%, 30-50%, and 50-100% for HCHO. Note that the cloud effects on the MAX-DOAS results are discussed in detail in section S2 of the supplement. The most important finding is that the cloud effects on MAX-DOAS results are negligible for the satellite validation activities.

1) NO_2

Figures 2a, b and c display scatter plots (and the parameters from the linear regressions) of the daily averaged NO_2 tropospheric VCDs derived from OMI, GOME-2A, and GOME-2B products versus those derived from the corresponding MAX-DOAS measurements for eCF < 10%. Generally higher correlation coefficients (R^2) for OMI than for GOME-2A/B are found. The systematic biases of the satellite data with respect to the MAX-DOAS data are quantified by the mean relative difference (MRD) calculated following Eq. 1:

$$\mathrm{MRD} = \frac{\sum_1^n {}^{(V_{s_i} - V_{M_i})}/_{V_{M_i}}}{n} \quad (1)$$

Here V_{s_i} and V_{M_i}represent the averaged TG VCDs from satellite observations and MAX-DOAS measurements on day i, respectively; n is the total number of the available days. The MRD is only 1% for OMI, and 27% and 30% for GOME-2A and B, respectively.

The R^2, slopes and intercepts of the linear regressions, and the MRD as well as the number of available days for the three satellite products are shown for the five eCF bins in Fig. 3. For OMI, R^2 decreases with increasing eCF; the slopes significantly change for eCF > 50% and the MRD drops to -40% for eCF > 40%. For GOME-2A, a steep decrease of R^2 for eCF > 30% is found. For GOME-2B, a generally lower R^2 is found for eCF >30%.; the MRD indicates an increasing systematic overestimation for eCF > 30%. Thus we conclude that the cloud effect on OMI and GOME-2A/B NO_2 data becomes significant for eCF >40% and 30%, respectively.

2) SO_2:

Figures 4a, b, c, d, and e display scatter plots of the daily averaged SO_2 tropospheric VCDs derived from the OMI NASA, OMI BIRA, GOME-2A DLR, GOME-2A and B BIRA products versus those derived from the corresponding MAX-DOAS measurements for eCF < 10%. R^2 and slopes are more close to unity for the OMI BIRA product than for the other products. The MRDs indicate a similar systematic underestimation (-40% to -52%) by all products. There are fewer negative values in the OMI BIRA product than in the other satellite products. It needs to be noted that the significantly worse R^2 for the OMI

NASA product compared to the OMI BIRA product could partly be attributed to the assumed fixed measurement condition (and thus the fixed AMF) in the NASA PCA retrievals. However the similar slopes and MRDs between the two OMI products indicate that the simplification of the NASA PCA retrieval only slightly contributes to the systematic bias of the averaged values.

The R^2, slopes and intercepts of the linear regressions, the MRD as well as the number of the available days obtained for the five satellite SO_2 products are shown for the five eCF bins in Fig. 5. For the OMI BIRA product, a significant decrease of R^2 occurs for eCF > 10% together with a decrease of the slopes and the MRD. A steep increase of the MRD is found for eCF > 40%. Therefore cloud effects on the OMI BIRA SO_2 data become considerable for eCF > 10%. For the OMI SO_2 NASA data, R^2, slope, and MRD significantly decrease for eCF > 20%. R^2 for both GOME-2A data are low (< 0.09) for all eCF bins, thus from the linear regressions no meaningful information on the cloud effect can be derived. Almost constant MRDs are found for both GOME-2A SO_2 products for eCF<30%. For eCF>30% largely varying MRD are found, especially for the GOME-2A BIRA products. Thus we conclude that the cloud effects on both GOME-2A products are appreciable for eCF > 30%. For the GOME-2B BIRA data, an obvious decrease of R^2 and slope is found for eCF > 10%, while for eCF>30% largely variable MRDs are found. Thus clouds can considerably impact the GOME-2B BIRA product for eCF > 10%, and more significantly for eCF > 30%.

3) HCHO:

Because of the rather small atmospheric absorption of HCHO, the DOAS fit errors often dominate the total uncertainty of the HCHO satellite data (De Smedt et al., 2015). Thus systematic effects, e.g. caused by clouds, are more difficult to identify and quantify than for NO_2 and SO_2. The scatter plot of the OMI HCHO VCDs for individual pixels versus those derived from MAX-DOAS observations for eCF < 30% are shown in Fig. 6. One important finding is that the R^2 for data with a fit error < 7×10^{15} molecules cm^{-2} is better than the R^2 for all data (see Fig. 6b). A similar result is obtained for the daily averaged OMI HCHO VCDs (see Fig. S12 in the supplement) indicating that the fit error dominates the random uncertainty of the HCHO VCDs derived from satellite. In contrast, the slopes of the linear regressions for the OMI data before and after the filtering are quite similar as shown in Fig. 6b and the supplementary Fig. S12. Thus the data screening has no considerable impact on the analysis of the systematic bias of the OMI HCHO products. Considering that the mean fit error of the HCHO VCDs is 7×10^{15} molecules cm^{-2} for the OMI data, for further comparisons, we exclude the HCHO VCDs with fit errors > 7×10^{15} molecules cm^{-2} for OMI. However for the GOME-2A/B products, the filter for the fit error is not applied because in contrast to the OMI HCHO data we find a systematic dependence of the fit error on the retrieved HCHO tropospheric VCD (see Fig. S13 in the supplement). The different findings with respect to the HCHO fit error for OMI and GOME-2 are not clearly understood and should be addressed in further investigations.

If the additional filter of the fit error for the OMI product is applied, 48% of the total number of HCHO data is left for comparisons. In order to still include a sufficient number of data, we use broader eCF bins (0-10%, 10%-30%, 30%-50% and 50%-100%). Figures 7a, c and d display scatter plots of the satellite daily averaged data versus the MAX-DOAS data for

eCF < 10% for OMI, GOME-2A, and GOME-2B data, respectively. We found the best consistency for the GOME-2B product probably because of the weaker degradation of GOME-2B during the short time after launch compared to OMI and GOME-2A. Nevertheless also other unknown reasons might play a role. One interesting finding is the better correlation of the OMI products for the eCF bin of 10% to 30% (see Fig. 7b) compared to the eCF < 10%. However, for eCF of 10% to 30% also a larger MRD of -34% (see Fig. 8) is found, which might be attributed to the effect of clouds, because the clear sky AMFs used in the retrievals for eCF < 10% (see the last paragraph of section 2.2) .

The dependencies of the results of the linear regressions and the MRDs on the eCFs are shown in Fig. 8 for the three satellite instruments. For OMI, a decrease of R^2 occurs for eCF > 30%, while for GOME-2A and GOME-2B, low R^2 are already found for eCF > 10%. Gradually increasing absolute values of the MRDs for all satellite instruments are found for increasing eCF. In general cloud effects on the HCHO products become substantial for eCF > 30% for the three satellite instruments. However it needs to be noted that our findings are derived for one location (Wuxi) and might not be fully representative for other locations. The use of the HCHO products with eCF < 40% is recommended by the retrieval algorithm developer (De Smedt et al., 2015).

3.2 Errors of shape factors from CTM and the effect on satellite VCD products

The shape factor (SF) is an input for the calculation of satellite AMF, which is needed to convert the SCD to the VCD (Palmer et al., 2001). Different retrieval algorithms acquire the SFs in different ways, mostly from a CTM for individual measurements or assuming a fixed SF (see section 2.2 and 2.3). The MAX-DOAS measurements acquire the vertical profiles of NO_2, SO_2 and HCHO from the ground up to the altitude of about 4km (depending on the measurement conditions), in which the tropospheric amounts of the TGs are mostly located. Thus the profiles derived from MAX-DOAS observations are valuable to evaluate the SFs used in the satellite retrievals and their effects on the AMFs and VCDs. Because the averaging kernels and SFs for individual satellite measurements are available only for the DOMINO NO_2, BIRA SO_2, and BIRA HCHO products derived from OMI observations, these three products are used to evaluate the effect of the SF in this section. For the three selected products, the calculation of the tropospheric satellite AMFs follows the same way as introduced in Palmer et al. (2001) as Eq. 2:

$$\mathrm{AMF} = \int_{ground}^{tropopause} BAMF(z)SF(z)dz \quad (2)$$

Here BAMF(z) is the box AMF, which characterizes the measurement sensitivity as a function of altitude (z). The integration is done from the ground to the tropopause. The SFs of the TGs are obtained from different CTM (TM4 for NO_2, IMAGES for SO_2 and HCHO, see section 2.2). The profiles ($\mathrm{profile}_M$) derived from MAX-DOAS can be converted to SF (SF_M) using Eq. 3:

$$\mathrm{SF}_M\,(\mathrm{z}) = \frac{\mathrm{profile}_M(\mathrm{z})}{VCD_M} \quad (3)$$

where VCD_M is the tropospheric VCD derived by an integration of the corresponding $\mathrm{profile}_M$. It needs to be noted that only the profiles below 4km can be reliably drawn from MAX-DOAS observations. Thus the $\mathrm{profile}_\mathrm{M}$ between 4km and the

tropopause (a fixed value of 16 km is used in this study) is derived from the corresponding CTM profiles of the individual satellite data sets. Therefore the SF_M is derived from the combined $profile_M$ using Eq.3. .

A similar relationship connects the BAMFs and averaging kernels (Eskes and Boersma, 2003):

$$AK(z) = \frac{BAMF(z)}{AMF} \quad (4)$$

The SF_M can replace the SF from CTM (SF_C) to recalculate the AMF using Eq. 2. A similar study was recently conducted by Theys et al. (2015) and De Smedt et al. (2015) for the OMI BIRA SO_2 and HCHO products over the Xianghe area. They demonstrated the improvements of the consistency between OMI VCDs and MAX-DOAS VCDs when using the SF_M for the AMF calculation of the satellite products by 20%-50%. In our study we follow the same procedure.

1) NO_2

The averaged NO_2 SF_C for the measurements under clear sky with eCF < 10%, is compared to SF_M in the altitude range of up to 4km in Fig. 9a. The differences between the averaged SF_C and SF_M shown in Fig. 9b indicate that in the layer below 4km for NO_2 SF_C is considerably larger than SF_M below 0.4 km and smaller above 0.4 km, respectively. In the altitude range above 4km SF_C is slightly larger than SF_M (see supplementary Fig. S14a). The OMI VCDs (VCD_{CTM}) retrieved with SF_C (directly derived from the DOMINO NO_2 product) and the modified OMI VCDs (VCD_{SM}) (based on SF_M and the NO_2 SCDs which are derived from the DOMINO NO_2 product) are plotted against the VCDs derived from MAX-DOAS observations in Fig. 9c. Very similar results for both VCD_{CTM} and VCD_{SM} are found. In Fig. 9e the relative differences of the AMFs using either SF_C (AMF_{CTM}) or SF_M ($AMF_{MAX-DOAS}$) are shown. The differences are calculated in two ways: either the relative differences are first calculated for individual measurements, and then the individual relative differences are averaged. Alternatively, first the AMFs of the individual measurements are averaged, and then the relative differences are calculated. The results in Fig. 9e show that also for both calculations very similar results are obtained. For eCF<10% the relative differences are only 0.3%. The small differences can be explained by a compensation effect of the negative and positive differences between SF_C and SF_M near the surface and at high altitudes, respectively..

For different eCF bins, the relative differences of AMF_{CTM} and $AMF_{MAX-DOAS}$ increase systematically with increasing eCF. This finding can be explained by the partial AMF above 4km (see supplementary Fig. S14c). The partial AMF_{CTM} is always larger than the partial $AMF_{MAX-DOAS}$ above 4km because SF_C is larger than SF_M. And the difference increases substantially with increasing eCF. Meanwhile the contribution of the partial AMF above 4km to the total tropospheric AMF increases with increasing eCF due to the strong decrease of the partial AMF below. Overall the overestimation of the partial AMF_{CTM} compared to the partial $AMF_{MAX-DOAS}$ above 4km becomes critical under cloudy conditions.

In general the TM4 NO_2 a-priori profile shapes agree well with the MAX-DOAS profiles, and the agreement with the MAX-DOAS VCDs by replacing SF_C with SF_M in the AMF calculation is only slightly improved for a small eCF. For large eCF, VCD_{SM} is systematically larger than VCD_{CTM} by 20% on average (see Fig. 3), consistent with the AMF differences shown in Fig. 9e.

2) SO_2

The results shown in Figures 10a and b indicate that in the layer below 4km for eCF < 10%, the SO_2 SF_C is considerably smaller than SF_M below 1 km and larger above 1 km, respectively. As can be seen in the supplementary Fig. S15a, SF_C is in general slightly larger than SF_M in the altitude range above 4km. Since the BAMFs increase with altitude (Fig. 10d) SO_2 AMF_{CTM} are on average larger than $AMF_{MAX-DOAS}$ by 18% (Fig. 10e). In contrast to NO_2, the SO_2 VCD_{SM} agree better with the MAX-DOAS VCDs than VCD_{CTM}, i.e. R^2 and slope increase from 0.47 to 0.60 and from 0.55 to 0.90, respectively (see Fig. 10c). Also the systematic bias of VCD_{SM} is smaller than that of VCD_{CTM}, i.e. the MRD is -26% for VCD_{SM} and -40% for VCD_{CTM} (see black and red curves in Fig. 5).

For different eCF bins, the differences between SO_2 SF_C and SF_M (Fig. 10b) as well as BAMFs (Fig. 10d) are slightly different from each other in the altitude range below 4km. However an obvious dependence of both quantities above 4km on eCF can be seen in supplementary Fig. S15a and b. The overestimation of SF_C compared to SF_M above 4km increases with increasing eCF, and the BAMF above 4km also increases with increasing eCF. Therefore the dependences of both quantities on eCF dominates the different levels of agreement of the partial AMF_{CTM} and partial $AMF_{MAX-DOAS}$ above 4km for different cloud conditions as shown in supplementary Fig. S15c. Furthermore, the partial AMF above 4km dominates the total tropospheric AMF for large eCF due to the decrease of the lower partial AMF with increasing eCF (see supplementary Fig. S15c). These dependencies of partial AMF_{CTM} and partial $AMF_{MAX-DOAS}$ above 4km on eCF also explain the dependencies of differences between the total tropospheric AMF_{CTM} and $AMF_{MAX-DOAS}$ on eCF as shown in Fig. 10e. However, in general the dependences on eCF is smaller than that for NO_2. In addition a better consistency between the SO_2 VCD_{SM} and the MAX-DOAS VCDs than for the VCD_{CTM} can be seen in Fig. 5 for all the eCF bins.

3) HCHO

The results shown in Fig. 11a and b indicate that in the altitude range below 4km for eCF < 10% the HCHO SF_C is considerably smaller below 1.7 km and larger than SF_M above 1.7 km, respectively. As can be seen in the supplementary Fig. S16a the SF_C almost equals the SF_M above 4km for eCF<10%. Since the BAMF increases with altitude (Fig. 11d) the HCHO AMF_{CTM} is on average larger than $AMF_{MAX-DOAS}$ by 11% (Fig. 11e). Like for SO_2 the VCD_{SM} agree better with the MAX-DOAS VCD than VCD_{CTM}, i.e. R^2 and slope increase from 0.15 to 0.21 and from 0.44 to 0.61, respectively (see Fig. 11c). Also the systematic bias of VCD_{SM} is smaller than that of VCD_{CTM}, i.e. the MRD is -10% for VCD_{SM} and -18% for VCD_{CTM} (see Fig. 8).

For different eCF bins, larger differences between AMF_{CTM} and $AMF_{MAX-DOAS}$ are found towards larger eCF (see Fig. 11e). Similar to NO_2 and SO_2, this finding is caused by the partial AMFs above 4km. The dependences of differences between HCHO SF_C and SF_M (Fig. 11b) as well as BAMFs (Fig. 11d) in the altitude range below 4km on eCF are insignificant. However both quantities above 4km obviously depend on eCF (see supplementary Fig. S16a and b). The overestimation of SF_C compared to SF_M above 4km increases with increasing eCF, and the BAMF above 4km also increases with increasing eCF. Therefore the dependences of both quantities on eCF dominate the different levels of agreement of the partial AMF_{CTM} and partial $AMF_{MAX-DOAS}$ above 4km for different cloud conditions as shown in supplementary Fig. S16c. Furthermore, the

partial AMF above 4km dominates the total tropospheric AMF for large eCF due to the decrease of the partial below 4km AMF with increasing eCF (see supplementary Fig. S16c). These dependencies of partial AMF_{CTM} and partial $AMF_{MAX-DOAS}$ above 4km on eCF also explain the dependencies of differences between the total tropospheric AMF_{CTM} and $AMF_{MAX-DOAS}$ on eCF as shown in Fig. 11e. In addition, figure 8 shows that for all the eCF bins the consistency between VCD_{SM} and the MAX-DOAS VCD is better than for VCD_{CTM}.

4) **Uncertainties of the SF from MAX-DOAS**

The previous study on the Wuxi MAX-DOAS observations (Wang et al., 2016) demonstrated that in general the profile retrievals are not sensitive to altitudes above 1-2km, where the retrieved profiles are strongly constrained to the a-priori profiles. Thus the SFs at high altitudes could be underestimated by MAX-DOAS retrievals. This effect could be considerable especially for SO_2 and HCHO, because they typically extend to higher altitudes than NO_2 (Xue et al., 2010, Junkermann, 2009 and Wagner et al., 2011). Because BAMFs of satellite observations are normally larger at high altitudes, the uncertainties of SFs from MAX-DOAS could cause an underestimation of $AMF_{MAX-DOAS}$, which further could cause an overestimation of VCD_{SM}. Since the profiles above 4km are not available from MAX-DOAS observation, they are taken from the corresponding CTM simulations for the different satellite data sets in this study. This procedure can contribute to an unknown error in the analysis of SF effects on satellite AMF and VCD calculations.

3.3 Comparisons of the bimonthly mean VCD

We calculate bi-monthly averaged tropospheric VCDs for eCF<30% for the coincident observations of the satellite instruments and MAX-DOAS (and also from the CTM simulations for the OMI products) from 2011 to 2014. The results for NO_2, SO_2 and HCHO are shown in Fig. 12. The numbers of available days for each satellite products are also shown in the bottom panels of each subfigure.

1) NO_2

For OMI good agreements with the MAX-DOAS VCDs are found both for the DOMINO and the improved VCDs using SFs from MAX-DOAS observations with a slightly better agreement for the improved VCDs. GOME-2A and B VCDs are systematically larger than the MAX-DOAS VCDs by about 5×10^{15} molecules cm^{-2} on average. The overestimation could be attributed to the errors of the NO_2 SFs from TM4 (Pinardi et al., 2013). Systematic differences between the GOME2-A and B VCDs are found, which can be partly explained by the different swath widths of both sensors after 15 July 2013. For the same reason also better agreement between GOME-2A and MAX-DOAS VCDs is found after summer 2013. The NO_2 VCDs simulated by TM4 for the OMI DOMINO v2 product are much smaller than those observed by satellite and MAX-DOAS. However the model data show a similar seasonality as the observational data. The significant underestimation of the TM4 NO_2 VCDs could be due to many factors, most importantly the limited spatial resolution of the model, which is especially relevant for species with strong horizontal gradients such as NO_2 and SO_2 (see Fig. 1). But also

possible errors in the emissions, transport schemes and/or chemical mechanisms might play a role. The determination of the specific contributions of the different error sources should be the subject of future studies.

2) SO_2

For SO_2 large differences between the absolute values of the satellite and MAX-DOAS results are found, but all data sets show a similar seasonality with minima in summer and maxima in winter. The best agreement with MAX-DOAS results is found for the OMI BIRA VCD_{SM}, which displays an almost identical magnitude of the SO_2 annual variation (while still showing a large bias). Interestingly, a much better agreement is found for the modified OMI SO_2 than for the OMI BIRA using the SF from the CTM. However the MAX-DOAS results are still significantly higher than the modified OMI products by about 1×10^{16} molecules cm^{-2} on average. Several reasons could contribute to the differences: 1) the horizontal gradient of SO_2 (see Fig. 1) and the MAX-DOAS pointing direction to the North can contribute to the differences of about 3×10^{15} molecules cm^{-2}. 2) The SO_2 cross section at 203K is applied in the current version of the OMI BIRA product. It was found that the temperature dependence of the SO_2 cross sections (Bogumil et al. 2003) should also be considered using e.g. a post-correction method (BIRA-IASB, 2016). The correction can increase SO_2 VCDs by up to 1×10^{16} molecules cm^{-2} with the highest absolute changes in winter. 3) The surface albedo used in the retrieval of the OMI BIRA product is taken from the climatological monthly minLER data from Kleipool et al. (2008) at 328 nm. We expect an uncertainty of the albedo of about 0.02. This will translate to an error of 15-20% of the SO_2 VCDs. 4) some unknown local emissions near the station might be underestimated by the satellite observations, but seen by the MAX-DOAS.

The BIRA GOME-2A/B and DLR GOME-2A data are well consistent with each other, but show large differences to the corresponding MAX-DOAS results. The SO_2 VCDs simulated by IMAGES are systematically lower than the MAX-DOAS observations and show only a low amplitude of the seasonal variation. Same as for TM4 NO_2, the discrepancy of the IMAGES SO_2 VCDs needs a further investigation in future studies.

3) HCHO

Relatively good agreement between the satellite and MAX-DOAS observations of HCHO is found for all data sets (except GOME-2A before summer 2013). For OMI a better agreement is found for the modified VCDs than for the original product, with a larger improvement in summer. GOME-2A/B products are consistent with each other but strongly underestimate the HCHO VCDs, especially in summer. It is interesting to note that the CTM results have a better consistency with the MAX-DOAS results than the OMI data. The much better consistency of the IMAGES HCHO VCDs compared to the SO_2 VCDs with MAX-DOAS measurements is also worth a further investigation in the future. It should be noted that GOME-2A data before summer 2013 show the largest disagreement with the MAX-DOAS data. The reason for this phenomenon is not clear, but might be related to the different swath width in that period.

3.4 Diurnal variations characterized by combining the GOME-2A/B and OMI observations and the weekly cycle

Because of the morning and afternoon overpass time of GOME-2 and OMI, respectively, several studies (e.g. Boersma et al., 2008; Lin et al., 2010; De Smedt et al., 2015) investigated the differences of both data sets to characterize the diurnal variations of the TGs. The diurnal variations can be attributed to the complex interaction of the primary and secondary emission sources, depositions, atmospheric chemical reactions, and transport processes. In this section we perform a similar study, but include also MAX-DOAS data coincident to the satellite observations. We calculate the ratios between the bi-monthly mean tropospheric VCDs from GOME-2A/B and OMI ($Ratio_{Sat}$) for each species and the corresponding ratios from the MAX-DOAS observations ($Ratio_{M-D}$). The results are shown in Fig. 13. The averaged $Ratio_{Sat}$ and $Ratio_{M-D}$ over the whole period are listed in Table 1. For NO_2, the $Ratio_{Sat}$ for both GOME-2 instruments show good agreement. Good agreement with the MAX-DOAS results is also found for the seasonal variation, but the absolute values differ. The systematic difference of $Ratio_{Sat}$ and $Ratio_{M-D}$ can be attributed to the known overestimation of the GOME-2 A/B tropospheric VCD compared to the MAX-DOAS results (see Fig. 12a). This finding also indicates that using GOME-2 and OMI data can lead to wrong conclusions about the diurnal cycles of NO_2. Also for the other trace gases we investigated the ratios between the different data sets. However, because of the larger uncertainties compared to NO_2, the conclusions for SO_2 and HCHO should be treated with care. For SO_2, although $Ratio_{Sat}$ shows several deviations from $Ratio_{M-D.}$, $Ratio_{M-D}$ and $Ratio_{Sat}$ are consistent on average and close to unity during a whole year indicating similar SO_2 VCDs around the overpass times of GOME-2 and OMI. For HCHO, on average good agreement between $Ratio_{Sat}$ and $Ratio_{M-D}$ is found for GOME-2A and GOME-2B (except some outliers of $Ratio_{Sat}$). Interestingly, both $Ratio_{Sat}$ and $Ratio_{M-D}$ are below unity indicating lower HCHO VCDs in the morning than in the afternoon.

We evaluate the weekly cycles of the VCDs of the TGs observed by satellite instruments and the corresponding MAX-DOAS. The weekly cycles are shown in the Fig. S17 in the supplement. In general only both GOME-2 instruments and the corresponding MAX-DOAS measurements observed a considerable weekly cycles for NO_2.

3.5 Aerosol effects on the satellite results

In this section the aerosol effects on the satellite products are investigated. The OMI products (for SO_2 the OMI BIRA product is used) are used for this study because of their better consistency with the MAX-DOAS results compared to the products of the other satellite instruments. In Fig. 14 the absolute (top) and relative (bottom) differences of the TG VCDs between OMI and MAX-DOAS observations for individual OMI pixels are plotted against the AODs at 360nm derived from the MAX-DOAS observations (Wang et al. 2016). It needs to be noted that the OMI VCDs used in Fig. 14 are the modified values using the SFs derived from MAX-DOAS observations in order to isolate the aerosol effects. The left subfigures show the comparisons for the data with eCF<10%, for which a potential cloud contamination is minimised. However the eCF filter can not exclude all clouds, and thus observations with thin cirrus clouds or other clouds with small geometric cloud fraction might still be included in the comparison, Therefore CTP > 900 hPa is used to further exclude residual clouds from the

comparisons. The comparisons for the data with eCF <10% and CTP>900 hPa are shown in the center part of Fig. 14. Finally also observations with small TG VCDs ($NO_2 < 2\times10^{16}$ molecules cm^{-2}, $SO_2 < 2\times10^{16}$ molecules cm^{-2}, and HCHO < 1×10^{16} molecules cm^{-2}) are skipped to minimise the influence of non-polluted observations on the comparison. The results after applying all three filters are shown in the right part of Fig. 14.

A systematically increasing underestimation of the OMI VCDs compared to MAX-DOAS VCDs with increasing AOD can been seen for NO_2 and SO_2. This indicates the effects of aerosols on the satellite products. However, here one aspect needs to be considered. Besides aerosols, also residual (low altitude) clouds might still have an effect on the comparison results. In order to quantify their potential effect, we performed RTM simulations (for details see section 3 in the supplement) to evaluate the difference of TG AMFs which are calculated for either aerosols or residual clouds. As residual clouds we chose either homogeneous optically thin clouds covering the whole satellite pixel or optically thick clouds covering only a small geometric fraction of the satellite pixel. For both types of clouds the extinction profiles were chosen to match the radiance and O_4 SCDs at 477nm of the aerosol cases. We found that the differences of the AMFs for aerosols and residual clouds are generally smaller than 10% for NO_2, and 5% for SO_2 and HCHO. It should be noted that the actual effect of residual clouds is in general much smaller, because usually aerosols and clouds are present at the same time. Thus we conclude that residual clouds have an negligible effect on the comparison results shown in Fig. 14 .

The dependence on AOD shown in Fig. 14 is strongest for NO_2. Besides the larger uncertainties of the HCHO and SO_2 retrievals, this is probably mainly related to the fact that in contrast to the DOMINO NO_2 product, for the OMI BIRA SO_2 and HCHO products no cloud correction is performed, i.e. a clear-sky AMF (for a Rayleigh scattering atmosphere) is applied in cases of eCF<10%.

Aerosols affect the satellite TG retrievals in two ways: First they affect the cloud retrievals of eCF and CTP and thus the TG AMFs if a cloud correction is applied in the satellite retrievals. If a Lambertian cloud model is used the effect of this implicit aerosol correction depends systematically on the aerosol properties. (Boersma et. al., 2011; Lin et al., 2014; Wang et al., 2015; Chimot et al., 2016). For mostly scattering aerosols at high altitudes the implicit aerosol correction can largely account for the aerosol effect on the TG products (Boersma et al., 2011). However in some important cases (for low altitude aerosols with high AOD and small SSA) the implicit correction might even increase the errors of the AMF Castellanos et al. (2015).

Besides the aerosol effect on the cloud retrievals and cloud correction schemes, aerosols also directly affect the AMF compared to AMFs for pure Rayleigh scattering conditions. Leitão et al. (2010) and Chimot et al., 2016 found that the influence of aerosols on the satellite retrievals mainly depends on the relative vertical distributions of aerosols and TGs. To further quantify both aerosol effects on the satellite retrievals we performed RTM simulations for typical scenarios of aerosols and TGs in Wuxi.

In Fig. 15 the OMI eCF and CTP (for eCF<10% and CTP>900hPa) are plotted against the AOD at 360nm derived from MAX-DOAS observation (similar plots for the AOD at 340nm derived from the nearby Taihu AERONET station (Holben et al. 1998, 2001) are shown in the supplementary Fig. S18). The results indicate a systematic increase of eCF and CTP with increasing AOD, but also a large scatter, especially for AOD <1. The systematic increase of eCF and CTP with AOD is

consistent with the model simulations in Chimot et al., 2016. The variability of eCF and CTP can be attributed to different observation geometries as well as uncertainties of the cloud retrievals (e.g. related to measurement uncertainties and/or the variability of surface properties). Also the frequency distributions of eCF and CTP are shown in Fig. 15. Considering and this frequency distribution and the variability of eCF and CTP, eCF of 5% and 10% as well as CTP of 900hPa and 1000hPa are used in the following for the RTM simulations to estimate the errors caused by aerosols. As aerosol properties we chose AOD values of 0.8 and 1.5, which represent typical and high aerosol loads at Wuxi, respectively. As vertical profile we chose an average profile derived from MAX-DOAS measurements under clear sky conditions (Wang et al., 2016), which is shown in the supplementary Fig. S19. The aerosol optical properties (single scattering albedo of 0.9 at 438nm, asymmetry parameter of 0.72 at 438nm, and Angstroem parameter of 0.85 at the wavelength pair of 340nm and 440nm) are taken from the AERONET observations at the nearby Taihu station (Holben et al. 1998, 2001). We use either shape factors (SFs) derived from the Wuxi MAX-DOAS observations or from the CTM simulations, which are also used for the satellite retrievals. The SFs of the TGs are shown in the supplementary Fig. S19. The surface albedo is set to 0.1 for NO_2 and 0.05 for SO_2 and HCHO simulations based on the averaged value of the surface reflectivity data base derived from OMI by Kleipool et al. (2008) over Wuxi station. Temperature and pressure profiles are derived from the US standard atmosphere data base. The RTM simulations are performed for five typical satellite observation geometries shown in Table 2. The TG BAMFs and AMFs were simulated for NO_2 at 435nm, HCHO at 337 nm and SO_2 at 319 nm using the RTM McArtim 3 (Deutschmann et al., 2011). Since the wavelength range covered by the AERONET measurements doesn't extend to the ultraviolet range, the same aerosol properties derived from the AERONET observations are used for the simulations at 319 nm (SO_2) and 337 nm (HCHO) and those at 435 nm (NO_2).

The simulations are performed for four scenarios: 1) pure Rayleigh scattering conditions ($BAMF_{clear\text{-}sky}$ and $AMF_{clear\text{-}sky}$); 2) aerosol profiles with the AOD of 0.8 and 1.5 ($BAMF_{explicit}$ and $AMF_{explicit}$); 3) Lambertian clouds at the surface (CTP of about 1000hPa) with an eCF of 10% and 5% ($BAMF_{low\text{-}cloud}$ and $AMF_{low\text{-}cloud}$); 4) Lambertian clouds at 1km (CTP of about 900hPa) with an eCF of 10% and 5% ($BAMF_{high\text{-}cloud}$ and $AMF_{high\text{-}cloud}$). The case 3 and 4 represent the implicit aerosol correction. Note that we use the same cloud model (Lambertian reflector with an albedo of 0.8) as in the official OMI cloud and TG retrievals.

The BAMFs for the different TGs simulated for the four scenarios at the g1 observation geometry (40 ° SZA, 180 ° RAA and 30 ° VZA) are shown in Fig. 16a. Note that the results of scenario 3 and 4 with eCF of 10% are shown. The relative differences of the BAMFs for clear sky and clouds compared to those explicitly considering aerosols (AOD of either 0.8 or 1.5) are shown in Fig. 16b and c, respectively. For all TGs, the clear sky BAMFs are higher close to the surface and lower for higher altitudes than the explicit aerosol BAMFs, which is caused by the additional aerosol scattering. The BAMFs near the surface for the cloud scenarios are either larger ('low cloud scenario') or smaller ('high cloud scenario') than the aerosol AMFs. For both cloud scenarios the BAMFs are higher than the aerosol BAMFs at higher altitudes. Overall the differences of the BAMFs for the cloud scenarios compared to the aerosol BAMFs are larger than the differences between the clear sky BAMFs and aerosol BAMFs. For the higher AOD (1.5) in general larger differences are found than for the small AOD (0.8).

The AMFs of NO_2, SO_2 and HCHO for the four scenarios are calculated using the corresponding BAMFs and typical SFs (shown in supplementary Fig. S19) derived from MAX-DOAS measurements and CTM simulations by Eq. 2. The relative differences of the AMFs for clear sky and for two cloud scenarios compared to the AMFs for the explicit aerosol simulations for five different satellite observation geometries (listed in Table 2) are shown in Fig. 17. Fig. 17a and b show the results for AOD of 0.8 and 1.5, respectively. It can be seen that the implicit aerosol correction can lead to large deviations, especially for the 'low cloud scenario'. The deviation for the 'high cloud scenario' is close to the deviation of clear sky AMF, and even smaller in some cases, due to the compensation of the partial AMF below and above the cloud plane. Here it should be noted that for aerosol layers reaching to higher altitudes the errors of the high cloud scenario will in general increase. For the 'low cloud scenario' the deviation increases with increasing eCF. As already seen for the BAMFs, also for the AMFs the deviations of the clear sky AMFs and Lambertian cloud AMFs increase with AOD. Overall the biases introduced by the implicit aerosol correction (3% to 85% for NO_2, -4% to 26% for HCHO, and -2% to 45% for SO_2) are significantly larger than those for the clear sky AMFs (5% to 50% for NO_2, -12% to -5% for HCHO, and -9% to 1% for SO_2). One important finding is that the stronger overestimation of the NO_2 AMF for the 'high cloud scenario' than for the 'low cloud scenario' as well as for eCF of 10% than 5% can well explain the observed dependence of the magnitude of the underestimation of the OMI NO_2 VCD on the CTP and eCF as shown in Fig. 14. Therefore we conclude that for measurements at Wuxi with strong aerosol loads, the implicit aerosol correction in general leads to larger biases of the derived TG VCDs than the use of a clear sky AMF.

4 Conclusions

Tropospheric VCDs of NO_2, SO_2, and HCHO derived from OMI, GOME-2A/B observations are validated using MAX-DOAS measurements in Wuxi, China from May 2011 to Dec 2014. Tropospheric VCDs and vertical profiles of aerosols and trace gases derived from the Wuxi MAX-DOAS observations using the PriAM OE-based algorithm are applied in this validation study.

We compare the daily averaged tropospheric VCDs from the satellite products with the corresponding MAX-DOAS results under clear sky conditions (eCF<10%). For NO_2 good agreement (R^2 of 0.73 and systematic bias of 1%) is found for the DOMINO v2 product. For both GOME-2 products (TM4NO2A) much weaker correlation (R^2 of 0.33 for GOME-2A and 0.2 for GOME-2B) is found with a similar systematic bias of about 30%. For SO_2 the OMI BIRA product shows a much better correlation (R^2 of 0.47) than the OMI NASA product (R^2=0.12), the GOME-2A BIRA product (R^2=0.07), the GOME-2A DLR product (R^2=0.09) and the GOME-2B BIRA product (r^2=0.28). All of these products systematically underestimate the SO_2 tropospheric VCDs by about 40% to 60%. For HCHO: the best agreement is found for the GOME-2B product with R^2 of 0.53 and a systematic bias of -12%. The OMI and GOME-2A products have lower R^2 of 0.17 and 0.18 with a similar systematic bias of about -20%, respectively.

In general, we expect that the VCDs from MAX-DOAS observations have much lower uncertainties than those from satellite observations. However we should also consider the total uncertainties of the MAX-DOAS VCDs of NO_2, SO_2, and HCHO of about 25%, 31% and 54%, respectively (Wang et al., 2016). Moreover, MAX-DOAS has low sensitivity to high altitudes, above about 1-2km. This can cause an underestimation of the VCDs retrieved from MAX-DOAS. The strength of this effect depends on the vertical distribution of the species, the atmospheric visibility, and the observation geometry of the MAX-DOAS measurement. In this study we do not discuss these issues in more detail. This should be done in further studies. Nevertheless, the sensitivity of MAX-DOAS observations to the boundary layer is much larger than for satellite observations, and this is the altitude range in which the pollutants are usually accumulated. Thus it is reasonable to assume that the systematic differences between both data sets are mainly attributed to the errors of the satellite observations.

We investigated the effects of clouds on the MAX-DOAS results and satellite products and find that the consistency (correlations and systematic bias) of satellite data with MAX-DOAS results deteriorates with increasing eCF. The cloud effects become significant for eCF > 40% for the OMI DOMINO NO_2 product, >30% for the GOME-2A\B NO_2 products, > 10% for the OMI BIRA SO_2 product, >20% for the OMI NASA SO_2 product, >30% for the GOME-2A/B BIRA SO_2 products and >30% for all HCHO products. Here it should be noted that except optically thick clouds and fog, the cloud effects on the MAX-DOAS results are negligible. It should also be noted that these findings are obtained for the original satellite products, namely using SF from CTM or assumed fixed SF. In addition, the different thresholds of eCF could also be related to the properties of the different cloud products. This effect is not discussed in this paper, and is valuable to be further studied. In general, it should be noted that these results are representative for conditions like in Wuxi, and might be different for other locations.

In the OMI DOMINO NO_2, OMI BIRA SO_2 and HCHO products, the a-priori SFs of the trace gases are obtained from CTM. We compare these SFs (derived from TM4 for NO_2, and IMAGES for SO_2 and HCHO) with those derived from MAX-DOAS observation and find substantial differences. We investigate the effect of using the MAX-DOAS SFs in the satellite retrievals. Under clear sky conditions, the application of the SFs from MAX-DOAS changes the SO_2 and HCHO AMFs by about 18% and 11%, respectively, but has almost no impact on the NO_2 AMFs. We find that the modified satellite VCDs based on the MAX-DOAS SF show much better agreement with the MAX-DOAS results (considerably higher correlation coefficients R^2 and smaller systematic biases) than the original satellite data. The improvement is strongest for periods with large trace gas VCDs, namely for NO_2 and SO_2 in winter and for HCHO in summer. In these periods, NO_2, SO_2 and HCHO VCD change by up to 10%, 47% and 35%, respectively. We also found that the effect of using the MAX-DOAS SFs in the satellite retrievals increases for increasing eCF. This finding is mainly caused by the partial satellite AMF above 4km and the significant reduction of the partial satellite AMF below 4km in cloudy situations. In addition, the low sensitivity of MAX-DOAS above about 1 - 2 km could cause an underestimation of the MAX-DOAS SFs of the trace gases at higher altitudes, especially for SO_2 and HCHO. This effect could cause the underestimation of the AMFs and an overestimation of the VCDs by using the MAX-DOAS SFs.

We also compare the bi-monthly mean satellite products to the corresponding MAX-DOAS results. The relative seasonal variations of the NO_2, SO_2, HCHO tropospheric VCDs from the different satellite products agree well with the corresponding MAX-DOAS results. The best consistency is found for the OMI DOMINO NO_2 product. A systematic overestimation of the NO_2 VCDs is found for GOME-2A\B NO_2 products. All SO_2 satellite products show similar SO_2 VCDs and a systematic underestimation of about 2×10^{16} molecules cm^{-2}. Based on the studies on the OMI BIRA product, the systematic underestimation could be attributed to a combined effect of errors of the SFs, horizontal gradients of the SO_2 distribution, the temperature dependence of the SO_2 cross section, and uncertainties of the surface albedo and local emissions. The OMI NASA, and the GOME-2A BIRA and DLR SO_2 products show a larger random variability than the OMI and GOME-2B BIRA SO_2 products. All OMI and GOME-2A/B products systematically underestimate the tropospheric HCHO VCDs by about 5×10^{15} molecules cm^{-2}, while showing a similar seasonality as the MAX-DOAS results. The biases found for the bimonthly averaged satellite TG VCDs are consistent with those found for the daily comparisons.

We compared the diurnal variations (ratios of morning and afternoon values) of TGs by combining GOME-2A/B (morning overpass) with OMI (afternoon overpass) observations with the corresponding MAX-DOAS observations. Generally higher NO_2 values and lower HCHO values in the morning are acquired, but no significant diurnal cycle was found for SO_2. Well consistent diurnal variations of HCHO and SO_2 between satellite and MAX-DOAS observations were derived. The combined satellite observations systematically overestimate the magnitude of the NO_2 diurnal variation compared to MAX-DOAS due to the overestimation of the NO_2 VCDs by GOME-2. In addition no significant weekly cycle was found for the three TGs in the satellite and MAX-DOAS data.

Finally we studied the effects of aerosols on the OMI products over the Wuxi station based on the MAX-DOAS observations. We find that the underestimation of the TG VCDs derived from satellite observations for mainly cloud-free observations compared to the MAX-DOAS observations systematically increases with AOD. We also investigate the aerosol effect based on RTM simulations. Here it is in particular possible to separate the aerosol effect into two contributions: a) the effect of using a clear sky AMF instead of an AMF taking explicitly into account the aerosol effects, and b) the effect of aerosols on the cloud retrievals, which are used in the satellite TG retrievals (implicit aerosol correction). We find that for the measurements affected by high aerosol loads in Wuxi, in general the effect of the implicit cloud correction on the retrieved TG VCDs is much stronger than the difference of a clear sky AMF compared to an AMF taking explicitly into account the aerosol extinction. We also showed that for eCF <10% and CTP >900hPa the effect of residual clouds can be neglected if aerosol extinction is explicitly taken into account. Moreover, the observed underestimation of the OMI NO_2 VCD for large AOD can be well explained by the error caused by the implicit aerosol correction. Therefore it might be reasonable to apply a clear-sky AMFs in the satellite retrievals of tropospheric TG VCDs in cases of low cloud altitudes (CTP > 900hPa) and low cloud fractions (eCF<10%) if explicit aerosol information is not available.

Acknowledgements: We thank Wuxi CAS Photonics Co. Ltd for their contributions in operating the MAX-DOAS instrument. We thank the Institute of Remote Sensing / Institute of Environmental Physics, University of Bremen, Bremen,

Germany for their freely accessible RTM SCIATRAN program. We thank Goddard Space Flight Center, NASA for their freely accessible archive of AERONET and MODIS data. We thank Prof. Ma Ronghua in Nanjing Institute of Geography & Limnology Chinese Academy of Sciences for his effort to operate the Taihu AERONET station. We thank the Royal Netherlands Meteorological Institute for their freely accessible archive of OMI tropospheric NO_2 data. This work was supported by Max Planck Society-Chinese Academy of Sciences Joint Doctoral Promotion Programme, and Monitoring and Assessment of Regional air quality in China using space Observations, Project Of Long-term sino-european co-Operation (MarcoPolo), FP7 (Grant No: 606953) and National Natural Science Foundation of China (Grant No.: 41275038).

References

Acarreta, J.R., De Haan, J.F. and Stammes, P.: Cloud pressure retrieval using the O_2 - O_2 absorption band at 477 nm. Journal of Geophysical Research: Atmospheres, 109(D5), 2004.

Barkley, M.P., Kurosu, T.P., Chance, K., De Smedt, I., Van Roozendael, M., Arneth, A., Hagberg, D. and Guenther, A.: Assessing sources of uncertainty in formaldehyde air mass factors over tropical South America: Implications for top - down isoprene emission estimates. *Journal of Geophysical Research: Atmospheres*, *117*(D13), 2012.

Bauwens, M., Stavrakou, T., Müller, J.-F., De Smedt, I., Van Roozendael, M., van der Werf, G. R., Wiedinmyer, C., Kaiser, J. W., Sindelarova, K., and Guenther, A.: Nine years of global hydrocarbon emissions based on source inversion of OMI formaldehyde observations, Atmos. Chem. Phys. Discuss., doi:10.5194/acp-2016-221, in review, 2016.

Beirle, S., Platt, U., Wenig, M., and Wagner, T.: Weekly cycle of NO_2 by GOME measurements: a signature of anthropogenic sources, Atmos. Chem. Phys., 3, 2225–2232, doi:10.5194/acp-3-2225-2003, 2003.

Beirle, S. and Wagner, T.: Tropospheric vertical column densities of NO_2 from SCIAMACHY, available at:http://www.sciamachy.org/products/NO2/NO2vcv09MPIAD.pdf(last access: Octo-ber 2012), 2010.

Beirle, S., Boersma, K. F., Platt, U., Lawrence, M. G., and Wagner, T.: Megacity emissions and lifetimes of nitrogen oxides probed from space, Science, 333, 1737–1739, 2011.

BIRA-IASB: S5P/TROPOMI SO2 ATBD, Issue 1.0.0, available at: http://www.tropomi.eu/sites/default/files/files/S5P-BIRA-L2-ATBD-SO2_400E_TROPOMI_v1p0p0_20160205.pdf, (last access: 26 July 2014), 2016.

Bobrowski, N., Honninger, G., Galle, B. and Platt, U.: Detection of bromine monoxide in a volcanic plume, Nature, 423, 273–276, 2003.

Boersma, K.F., H.J. Eskes and E.J. Brinksma, Error Analysis for Tropospheric NO_2 Retrieval from Space, J. Geophys. Res. 109 D04311, doi:10.1029/2003JD003962, 2004

Boersma, K. F., Eskes, H. J., Veefkind, J. P., Brinksma, E. J., van der A, R. J., Sneep, M., van den Oord, G. H. J., Levelt, P. F., Stammes, P., Gleason, J. F., and Bucsela, E. J.: Near-real time retrieval of tropospheric NO2 from OMI, Atmos. Chem. Phys., 7, 2103-2118, doi:10.5194/acp-7-2103-2007, 2007.

Boersma, K. F., Jacob, D. J., Eskes, H. J., Pinder, R. W., and Wang, J.: Intercomparison of SCIAMACHY and OMI tropospheric NO2 columns: Observing the diurnal evolution of chemistry and emissions from space, J. Geophys. Res., 113, D16S26, doi:10.1029/2007JD008816, 2008

Boersma, K.F., H.J. Eskes, R. J. Dirksen, R. J. van der A, J. P. Veefkind, P. Stammes, V. Huijnen, Q. L. Kleipool, M. Sneep, J. Claas, J. Leitao, A. Richter, Y. Zhou, and D. Brunner, An improved retrieval of tropospheric NO_2 columns from the Ozone Monitoring Instrument, Atmos. Meas. Tech. , 4, 1905-1928, 2011

Bogumil, K., Orphal, J., Homann, T., Voigt, S., Spietz, P., Fleischmann, O. C., Vogel, A., Hart-mann, M., Kromminga, H., Bovensmann, H., Frerick, J., and Burrows, J. P.: Measurements of molecular absorption spectra with the SCIAMACHY pre-flight model: instrument characterization and reference data for atmospheric remote-sensing in the 230–2380 nm region, J. Photoch. Photobio. A, 157, 167–184, 2003.

Bovensmann, H., Burrows, J. P., Buchwitz, M., Frerick, J., Noël, S., Rozanov, V. V., Chance, K. V., and Goede, A. P. H.: SCIA-MACHY: Mission objectives and measurement modes, J. Atmos. Sci., 56, 127–150, 1999.

Brinksma, E. J., Pinardi, G., Volten, H., Braak, R., Richter, A., Schönhardt, A., van Roozendael, M., Fayt, C., Hermans, C., Dirksen, R. J., Vlemmix, T., Berkhout, A. J. C., Swart, D. P. J., Oetjen, H., Wittrock, F., Wagner, T., Ibrahim, O. W., de Leeuw, G., Moerman, M., Curier, R. L., Celarier, E. A., Cede, A., Knap, W. H., Veefkind, J. P., Eskes, H. J., Allaart, M., Rothe, R., Piters, A. J. M., and Levelt, P. F.: The 2005 and 2006 DANDELIONS NO_2 and aerosol intercomparison campaigns, J. Geophys. Res., 113, D16S46, 2008.

Burrows, J.P., Weber, M., Buchwitz, M., Rozanov, V., Ladstätter-Weißenmayer, A., Richter, A., DeBeek, R., Hoogen, R., Bramstedt, K., Eichmann, K.U. and Eisinger, M.: The global ozone monitoring experiment (GOME): Mission concept and first scientific results, Journal of the Atmospheric Sciences, 56(2), pp.151-175, 1999

Cahalan, R. F., W. Ridgway, W. J. Wiscombe, S. Gollmer, and Harshvardhan: Independent pixel and Monte Carlo estimates of stratocumulus albedo, J. Atmos. Sci., 3776, 1994.

Callies, J., Corpaccioli, E., Eisinger, M., Hahne, A., and Lefebvre, A.: GOME-2 – MetOp's Second Generation Sensor for Opera-tional Ozone Monitoring, ESA Bulletin, 102, 28–36, 2000.

Carn, S.A., Krueger, A.J., Krotkov, N.A. and Gray, M.A.: Fire at Iraqi sulfur plant emits SO2 clouds detected by Earth Probe TOMS. Geophysical research letters, 31(19), 2004.

Castellanos, P., Boersma, K. F., Torres, O., and de Haan, J. F.: OMI tropospheric NO2 air mass factors over South America: effects of biomass burning aerosols, Atmos. Meas. Tech., 8, 3831-3849, doi:10.5194/amt-8-3831-2015, 2015.

Celarier, E.A., Brinksma, E.J., Gleason, J.F., Veefkind, J.P., Cede, A., Herman, J.R., Ionov, D., Goutail, F., Pommereau, J.P., Lambert, J.C. and Van Roozendael, M.: Validation of Ozone Monitoring Instrument nitrogen dioxide columns. Journal of Geophysical Research: Atmospheres,113(D15), 2008

Chance, K., Palmer, P. I., Spurr, R. J., Martin, R. V., Kurosu, T. P., and Jacob D. J.: Satellite observations of formaldehyde over North America from GOME, Geophys. Res. Lett., 27, 3461–3464, 2000.

Chan, K. L., Hartl, A., Lam, Y. F., Xie, P. H., Liu, W. Q., Cheung, H. M., Lampel, J., Pöhler, D., Li, A., Xu, J., Zhou, H. J., Ning, Z. Wenig, M. O.: Observations of tropospheric NO_2 using ground based MAX-DOAS and OMI measurements during the Shanghai World Expo 2010, Atmospheric Environment, 119, 45-58, 2015

Chen, D., Zhou, B., Beirle, S., Chen, L. M., and Wagner, T.: Tropospheric NO_2 column densities deduced from zenith-sky DOAS measurements in Shanghai, China, and their application to satellite validation, Atmos. Chem. Phys., 9, 3641-3662, 2009.

Chimot, J., Vlemmix, T., Veefkind, J. P., de Haan, J. F., and Levelt, P. F.: Impact of aerosols on the OMI tropospheric NO_2 retrievals over industrialized regions: how accurate is the aerosol correction of cloud-free scenes via a simple cloud model?, Atmos. Meas. Tech., 9, 359-382, doi:10.5194/amt-9-359-2016, 2016.

Clemer, K., Van Roozendael, M., Fayt, C., Hendrick, F., Hermans, C., Pinardi, G., Sperr, R., Wang, P., and De Maziere, M.: Multiple wavelength retrieval of tropospheric aerosol optical properties from MAXDOAS measurements in Beijing, Atmos. Meas. Tech., 3, 863–878, 2010.

Crippa, M., Ciarelli, G., Piazzalunga, A., Schwikowski, M., Abbaszade, G., Schnelle-Kreis, J., Zimmermann, R., An, Z., Szidat, S., Baltensperger, U., El Haddad, I., and Prevot, A. S.: High secondary aerosol contribution to particulate pollution during haze events in China, Nature, 514, 218–222, 2014.

De Smedt, I., Müller, J.-F., Stavrakou, T., van der A, R., Eskes, H., and Van Roozendael, M.: Twelve years of global observations of formaldehyde in the troposphere using GOME and SCIAMACHY sensors, Atmos. Chem. Phys., 8, 4947–4963, doi:10.5194/acp-8-4947-2008, 2008.

De Smedt, I., Van Roozendael, M., Stavrakou, T., Müller, J.-F., Lerot, C., Theys, N., Valks, P., Hao, N., and van der A, R.: Improved retrieval of global tropospheric formaldehyde columns from GOME-2/MetOp-A addressing noise reduction and instru-mental degradation issues, Atmos. Meas. Tech., 5, 2933–2949, doi:10.5194/amt-5-2933-2012, 2012.

De Smedt, I., Stavrakou, T., Hendrick, F., Danckaert, T., Vlemmix, T., Pinardi, G., Theys, N., Lerot, C., Gielen, C., Vigouroux, C., Hermans, C., Fayt, C., Veefkind, P., Müller, J.-F., and Van Roozendael, M.: Diurnal, seasonal and long-term variations of global formaldehyde columns inferred from combined OMI and GOME-2 observations, Atmos. Chem. Phys., 15, 12519-12545, doi:10.5194/acp-15-12519-2015, 2015.

Deutschmann, T., Beirle, S., Frieß, U., Grzegorski, M., Kern, C., Kritten, L., Platt, U., Prados-Román, C., Puķı, J., Wagner, T. and Werner, B.: The Monte Carlo atmospheric radiative transfer model McArtim: Introduction and validation of Jacobians and 3D features, Journal of Quantitative Spectroscopy and Radiative Transfer, 112(6), 1119-1137, 2011.

Dirksen, R. J., Boersma, K. F., Eskes, H. J., Ionov, D. V., Bucsela, E. J., Levelt, P. F., and Kelder, H. M.: Evaluation of stratospheric NO_2 retrieved from the Ozone Monitoring Instrument: intercomparison, diurnal cycle and trending, J. Geophys. Res., 116, D08305, doi:10.1029/2010JD014943, 2011.

Ding, J., van der A, R. J., Mijling, B., Levelt, P. F., and Hao, N.: NOx emission estimates during the 2014 Youth Olympic Games in Nanjing, Atmos. Chem. Phys., 15, 9399-9412, doi:10.5194/acp-15-9399-2015, 2015.

Eisinger, M. and Burrows, J.P.: Tropospheric sulfur dioxide observed by the ERS-2 GOME instrument. Geophysical Research Letters, 25(22), pp.4177-4180, 1998.

Environmental Protection Agency: National air quality and emissions trends report 1998, Rep. EPA 454/R-00-003, 1998.

Eskes, H. J., and Boersma, K. F.: Averaging kernels for DOAS total-column satellite retrievals, Atmos. Chem. Phys., 3, 1285-1291, 10.5194/acp-3-1285-2003, 2003.

Frieß, U., Monks, P. S., Remedios, J. J., Rozanov A., Sinreich R., Wagner T., and Platt, U.: MAX-DOAS O4 measurements: A new technique to derive information on atmospheric aerosols: 2. Modeling studies, J. Geophys. Res., 111, D14203, 2006, doi:10.1029/2005JD006618.

Frieß U, Sihler H, Sander R. The vertical distribution of BrO and aerosols in the Arctic: Measurements by active and passive differential optical absorption spectroscopy, J. Geophys. Res., 116, D00R04, 2011.

Frieß, U., Klein Baltink, H., Beirle, S., Clèmer, K., Hendrick, F., Henzing, B., Irie, H., de Leeuw, G., Li, A., Moerman, M. M., van Roozendael, M., Shaiganfar, R., Wagner, T., Wang, Y., Xie, P., Yilmaz, S., and Zieger, P.: Intercomparison of aerosol extinction profiles retrieved from MAX-DOAS measurements, Atmos. Meas. Tech. Discuss., doi:10.5194/amt-2015-358, 2016.

Fu, G. Q., Xu, W. Y., Yang, R. F., Li, J. B., and Zhao, C. S.: The distribution and trends of fog and haze in the North China Plain over the past 30 years, Atmos. Chem. Phys., 14, 11949-11958, doi:10.5194/acp-14-11949-2014, 2014.

González Abad, G., Liu, X., Chance, K., Wang, H., Kurosu, T. P., and Suleiman, R.: Updated Smithsonian Astrophysical Observatory Ozone Monitoring Instrument (SAO OMI) formaldehyde retrieval, Atmos. Meas. Tech., 8, 19-32, doi:10.5194/amt-8-19-2015, 2015.

Gonzi, S., Palmer, P.I., Barkley, M.P., De Smedt, I. and Van Roozendael, M.: Biomass burning emission estimates inferred from satellite column measurements of HCHO: Sensitivity to co‐emitted aerosol and injection height. Geophysical Research Letters, 38(14), 2011.

Hains, J. C., Boersma, K. F., Kroon, M., Dirksen, R. J., Cohen, R. C., Perring, A. E., Bucsela, E., Volten, H., Swart, D. P. J., Richter, A., Wittrock, F., Shoenhardt, A., Wagner, T., Ibrahim, O. W., Van Roozendael, M., Pinardi, G., Gleason, J. F., Veefkind, J. P., and Levelt, P.: Testing and improving OMI DOMINO tropospheric NO_2 using observations from the DANDELIONS and INTEX-B validation campaigns, J. Geophys. Res., 115, D05301, doi:10.1029/2009JD012399, 2010.

Han, K. M., Lee, S., Chang, L. S., and Song, C. H.: A comparison study between CMAQ-simulated and OMI-retrieved NO2columns over East Asia for evaluation of NOx emission fluxes of INTEX-B, CAPSS, and REAS inventories, Atmos. Chem. Phys., 15, 1913-1938, doi:10.5194/acp-15-1913-2015, 2015.

Hartl, A. and Wenig, M. O.: Regularisation model study for the least-squares retrieval of aerosol extinction time series from UV/VIS MAX-DOAS observations for a ground layer profile parameterisation, Atmos. Meas. Tech., 6, 1959-1980, doi:10.5194/amt-6-1959-2013, 2013.

Hassinen, S., Balis, D., Bauer, H., Begoin, M., Delcloo, A., Eleftheratos, K., Gimeno Garcia, S., Granville, J., Grossi, M., Hao, N., Hedelt, P., Hendrick, F., Hess, M., Heue, K.-P., Hovila, J., Jønch-Sørensen, H., Kalakoski, N., Kauppi, A.,

Kiemle, S., Kins, L., Koukouli, M. E., Kujanpää, J., Lambert, J.-C., Lang, R., Lerot, C., Loyola, D., Pedergnana, M., Pinardi, G., Romahn, F., van Roozendael, M., Lutz, R., De Smedt, I., Stammes, P., Steinbrecht, W., Tamminen, J., Theys, N., Tilstra, L. G., Tuinder, O. N. E., Valks, P., Zerefos, C., Zimmer, W., and Zyrichidou, I.: Overview of the O3M SAF GOME-2 operational atmospheric composition and UV radiation data products and data availability, Atmos. Meas. Tech., 9, 383-407, doi:10.5194/amt-9-383-2016, 2016.

Heckel, A., Kim, S.-W., Frost, G. J., Richter, A., Trainer, M., and Burrows, J. P.: Influence of low spatial resolution a priori data on tropospheric NO_2 satellite retrievals, Atmos. Meas. Tech., 4, 1805–1820, doi:10.5194/amt-4-1805-2011, 2011.

Herron-Thorpe, F. L., Lamb, B. K., Mount, G. H., and Vaughan, J. K.: Evaluation of a regional air quality forecast model for tropospheric NO2 columns using the OMI/Aura satellite tropospheric NO2 product, Atmos. Chem. Phys., 10, 8839-8854, doi:10.5194/acp-10-8839-2010, 2010.

Hewson, W., Bösch, H., Barkley, M. P., and De Smedt, I.: Charac-terisation of GOME-2 formaldehyde retrieval sensitivity, Atmos. Meas. Tech., 6, 371–386, doi:10.5194/amt-6-371-2013, 2013.

Holben, B. N., Eck, T. F., Slutsker, I., Tanre, D., Buis, J. P., Set-zer, A., Vermote, E., Reagan, J. A., Kaufman, Y., Nakajima, T., Lavenu, F., Jankowiak, I., and Smirnov, A.: AERONET – A federated instrument network and data archive for aerosol characterization, Remote Sens. Environ., 66, 1–16, 1998.

Holben, B. N., Tanre, D., Smirnov, A., Eck, T. F., Slutsker, I., Abuhassan, N., Newcomb, W. W., Schafer, J., Chatenet, B., Lav-enue, F., Kaufman, Y. J., Van de Castle, J., Setzer, A., Markham, B., Clark, D., Frouin, R., Halthore, R., Karnieli, A., O'Neill, N. T., Pietras, C., Pinker, R. T., Voss, K., and Zibordi, Z.: An emerging ground-based aerosol climatology: Aerosol optical depth from AERONET, J. Geophys. Res., 106, 12067–12097, 2001

Hönninger, G. and Platt, U.: Observations of BrO and its vertical distribution during surface ozone depletion at Alert, Atmos. Environ., 36, 2481–2489, 2002.Hönninger, G., Friedeburg, C. von and Plat, U., Multi axis differential optical absorption spectroscopy (MAX-DOAS), Atmos. Chem. Phys., 4, 231–254, 2004

Huang, R.-J., Zhang, Y., Bozzetti, C., Ho, K.-F., Cao, J., Han, Y., Dällenbach, K. R., Slowik, J. G., Platt, S. M., Canonaco, F., Zotter, P., Wolf, R., Pieber, S. M., Bruns, E. A., Crippa, M., Ciarelli, G., Piazzalunga, A., Schwikowski, M., Abbaszade, G., Schnelle-Kreis, J., Zimmermann, R., An, Z., Szidat, S., Baltensperger, U., Haddad, I. E., and Prévôt, A. S. H.: High secondary aerosol contribution to particulate pollution during haze events in China, Nature, 514, 218–222, 2014.

Irie, H., Kanaya, Y., Akimoto, H., Iwabuchi, H., Shimizu, A., and Aoki, K.: First retrieval of tropospheric aerosol profiles using MAX-DOAS and comparison with lidar and sky radiometer measurements, Atmos. Chem. Phys., 8, 341–350, 2008.

Irie, H., Takashima, H., Kanaya, Y., Boersma, K. F., Gast, L., Wittrock, F., Brunner, D., Zhou, Y., and Van Roozendael, M.: Eight-component retrievals from ground-based MAX-DOAS observations, Atmos. Meas. Tech., 4, 1027–1044, 2011.

Irie, H., Boersma, K. F., Kanaya, Y., Takashima, H., Pan, X., and Wang, Z. F.: Quantitative bias estimates for tropospheric NO_2 columns retrieved from SCIAMACHY, OMI, and GOME-2 using a common standard for East Asia, Atmos. Meas. Tech., 5, 2403-2411, doi:10.5194/amt-5-2403-2012, 2012.

Irie, H., Muto, T., Itahashi, S., Kurokawa, J.I. and Uno, I.: Turnaround of Tropospheric Nitrogen Dioxide Pollution Trends in China, Japan, and South Korea, SOLA, 12(0), 170-174, doi:10.2151/sola.2016-035, 2016.

Jiang, C., Wang, H., Zhao, T., Li, T., and Che, H.: Modeling study of PM2.5 pollutant transport across cities in China's Jing–Jin–Ji region during a severe haze episode in December 2013, Atmos. Chem. Phys., 15, 5803-5814, doi:10.5194/acp-15-5803-2015, 2015.

Jin, J., Ma, J., Lin, W., Zhao, H., Shaiganfar, R., Beirle, S. and Wagner, T.: MAX-DOAS measurements and satellite validation of tropospheric NO_2 and SO_2 vertical column densities at a rural site of North China. Atmospheric Environment, 133, pp.12-25, 2016.

Junkermann, W.: On the distribution of formaldehyde in the western Po-Valley, Italy, during FORMAT 2002/2003, Atmos. Chem. Phys., 9, 9187-9196, doi:10.5194/acp-9-9187-2009, 2009.

Kanaya, Y., Irie, H., Takashima, H., Iwabuchi, H., Akimoto, H., Sudo, K., Gu, M., Chong, J., Kim, Y. J., Lee, H., Li, A., Si, F., Xu, J., Xie, P.-H., Liu, W.-Q., Dzhola, A., Postylyakov, O., Ivanov, V., Grechko, E., Terpugova, S., and Panchenko, M.: Long-term MAX-DOAS network observations of NO2 in Russia and Asia (MADRAS) during the period 2007–2012: instrumentation, elucidation of climatology, and comparisons with OMI satellite observations and global model simulations, Atmos. Chem. Phys., 14, 7909-7927, doi:10.5194/acp-14-7909-2014, 2014.

Kaufman, Y. J., Tanré, D. and Boucher, O.: A satellite view of aerosols in the climate system. Nature, 419, 215-223, 2002

Khokhar, M.F., Frankenberg, C., Van Roozendael, M., Beirle, S., Kühl, S., Richter, A., Platt, U. and Wagner, T., Satellite observations of atmospheric SO_2 from volcanic eruptions during the time-period of 1996–2002. Advances in Space Research, 36(5), pp.879-887, 2005.

Kleipool, Q. L., Dobber, M.R., de Haan, J. and Levelt, P.F.: Earth surface reflectance climatology from 3 years of OMI data. Journal of Geophysical Research: Atmospheres, 113(D18), 2008.

Koukouli, M.E., Balis, D.S., Theys, N., Hedelt, P., Richter, A., Krotkov, N., Li, C. and Taylor, M.: Anthropogenic sulphur dioxide load over China as observed from different satellite sensors. Atmospheric Environment, 145, 45-59, 2016.

Krotkov, N.A., Carn, S.A., Krueger, A.J., Bhartia, P.K. and Yang, K.: Band residual difference algorithm for retrieval of SO_2 from the Aura Ozone Monitoring Instrument (OMI). Geoscience and Remote Sensing, IEEE Transactions on, 44(5), pp.1259-1266, 2006.

Krotkov, N.A., McClure, B., Dickerson, R.R., Carn, S.A., Li, C., Bhartia, P.K., Yang, K., Krueger, A.J., Li, Z., Levelt, P.F. and Chen, H.: Validation of SO_2 retrievals from the Ozone Monitoring Instrument over NE China. Journal of Geophysical Research: Atmospheres, 113(D16), 2008

Krueger, A.J., Walter, L.S., Bhartia, P.K., Schnetzler, C.C., Krotkov, N.A., Sprod, I.T. and Bluth, G.J.S.: Volcanic sulfur dioxide measurements from the total ozone mapping spectrometer instruments. Journal of Geophysical Research: Atmospheres, 100(D7), pp.14057-14076, 1995.

Kurosu, T. P.: OMHCHO README FILE, available at: https://www.cfa.harvard.edu/atmosphere/Instruments/OMI/PGEReleases/READMEs/OMHCHO_README.pdf (last access: 22 April 2016), 2008.

Lee, C., Martin, R.V., van Donkelaar, A., O'Byrne, G., Krotkov, N., Richter, A., Huey, L.G. and Holloway, J.S.: Retrieval of vertical columns of sulfur dioxide from SCIAMACHY and OMI: Air mass factor algorithm development, validation, and error analysis. Journal of Geophysical Research: Atmospheres, 114(D22), 2009

Leitão, J., Richter, A., Vrekoussis, M., Kokhanovsky, A., Zhang, Q. J., Beekmann, M., and Burrows, J. P.: On the improvement of NO2 satellite retrievals – aerosol impact on the airmass factors, Atmos. Meas. Tech., 3, 475-493, doi:10.5194/amt-3-475-2010, 2010.

Levelt, P. F., Hilsenrath, E., Lepppelmeier, G. W., van den Oord, G. H. J., Bhartia, P. K., Taminnen, J., de Haan, J. F., and Veefkind, J. P.: Science objectives of the Ozone Monitoring Instrument, IEEE Trans. Geosci. Remote Sens., 44, 1199–1208, 2006a.

Levelt, P. F., van den Oord, G. H. J., Dobber, M. R., Malkki, A., Visser, H., de Vries, J., Stammes, P., Lundell, J., and Saari, H.: The Ozone Monitoring Instrument, IEEE Trans. Geosci. Remote Sens., 44, 1093–1101, 2006b.

Li X., Brauers, T. and Hofzumahaus, A.: MAX-DOAS measurements of NO2, HCHO and CHOCHO at a rural site in Southern China. Atmos. Chem. Phys. Discuss., 12, 3983-4029, 2012.

Li X., Brauers, T., Shao, M., Garland, R. M., Wagner, T., Deutschmann, T., and Wahner, A.: MAX-DOAS measurements in southern China: retrieval of aerosol extinctions and validation using ground-based in-situ data. Atmos. Chem. Phys., 10, 2079–2089, 2010.

Li, C., Joiner, J., Krotkov, N.A. and Bhartia, P.K.: A fast and sensitive new satellite SO_2 retrieval algorithm based on principal component analysis: Application to the ozone monitoring instrument. Geophysical Research Letters, 40(23), 6314-6318, 2013.

Lin, J.-T., McElroy, M. B., and Boersma, K. F.: Constraint of anthropogenic NOx emissions in China from different sectors: a new methodology using multiple satellite retrievals, Atmos. Chem. Phys., 10, 63–78,doi:10.5194/acp-10-63-2010, 2010.

Lin, J.-T., Martin, R. V., Boersma, K. F., Sneep, M., Stammes, P., Spurr, R., Wang, P., Van Roozendael, M., Clémer, K., and Irie, H.: Retrieving tropospheric nitrogen dioxide from the Ozone Monitoring Instrument: effects of aerosols, surface reflectance anisotropy, and vertical profile of nitrogen dioxide, Atmos. Chem. Phys., 14, 1441-1461, doi:10.5194/acp-14-1441-2014, 2014.

Lin, J.-T., Liu, M.-Y., Xin, J.-Y., Boersma, K. F., Spurr, R., Martin, R., and Zhang, Q.: Influence of aerosols and surface reflectance on satellite NO2 retrieval: seasonal and spatial characteristics and implications for NOx emission constraints, Atmos. Chem. Phys., 15, 11217-11241, doi:10.5194/acp-15-11217-2015, 2015.

Lohmann, U., and Feichter, J.: Global indirect aerosol effects: a review, Atmos. Chem. Phys., 5, 715-737, 10.5194/acp-5-715-2005, 2005.

Loyola, D., W. Thomas, Y. Livschitz, T. Ruppert, P. Albert, and R. Hollmann: Cloud properties derived from GOME/ERS-2 backscatter data for trace gas retrieval,IEEE Trans. Geosci. Remote Sens. , 45(9), 2747 –2758, doi:10.1109/TGRS.2007.901043, 2007.

Ma, J. Z., Beirle, S., Jin, J. L., Shaiganfar, R., Yan, P., and Wagner, T.: Tropospheric NO2 vertical column densities over Beijing: results of the first three years of ground-based MAX-DOAS measurements (2008–2011) and satellite validation, Atmos. Chem. Phys., 13, 1547-1567, doi:10.5194/acp-13-1547-2013, 2013.

Martin, R. V., Jacob, D. J., Chance, K., Kurosu, T. P., Palmer, P. I., and Evans, M. J.: Global inventory of nitrogen oxide emis-sions constrained by space-based observations of NO_2 columns, J. Geophys. Res., 108, 4537,doi:10.1029/2003jd003453, 2003.

McCormic, R. A. and Ludwig, J. H.: Climate modifications by atmospheric aerosols, Science, 156, 1358–1359, 1967.

Millet, D. B., Jacob, D. J., Boersma, K. F., Fu, T.-M., Kurosu, T. P., Chance, K. V., Heald, C. L., and Guenther, A.: Spatial distri-bution of isoprene emissions from North America derived from formaldehyde column measurements by the OMI satellite sensor, J. Geophys. Res., 113, 1–18, doi:10.1029/2007JD008950, 2008.

Müller, J.F. and Brasseur, G.: IMAGES: A three−dimensional chemical transport model of the global troposphere. Journal of Geophysical Research: Atmospheres, 100(D8), pp.16445-16490, 1995.

Munro, R., Eisinger, M., Anderson, C., Callies, J., Corpaccioli, E., Lang, R., Lefebvre, A., Livschitz, Y., and Perez Albinana, A.: GOME-2 on MetOp: From in-orbit verification to routine oper-ations, in: Proceedings of EUMETSAT Meteorological Satellite Conference, Helsinki, Finland, 12–16 June 2006.

Munro, R., Lang, R., Klaes, D., Poli, G., Retscher, C., Lindstrot, R., Huckle, R., Lacan, A., Grzegorski, M., Holdak, A., Kokhanovsky, A., Livschitz, J., and Eisinger, M.: The GOME-2 instrument on the Metop series of satellites: instrument design, calibration, and level 1 data processing – an overview, Atmos. Meas. Tech., 9, 1279-1301, doi:10.5194/amt-9-1279-2016, 2016.

Nowlan, C.R., Liu, X., Chance, K., Cai, Z., Kurosu, T.P., Lee, C. and Martin, R.V., 2011. Retrievals of sulfur dioxide from the Global Ozone Monitoring Experiment 2 (GOME-2) using an optimal estimation approach: Algorithm and initial validation. Journal of Geophysical Research: Atmospheres, 116(D18), 2011

Ozone Monitoring Instrument (OMI), IEEE Trans. Geosci. Remote

Palmer, P. I., Jacob, D. J., Chance, K. V., Martin, R. V. D. R. J., Kurosu, T. P., Bey, I., Yantosca, R. M., and Fiore, A. M.: Air mass factor formulation for spectroscopic measurements from satellites: Application to formaldehyde retrievals from the Global Ozone Monitoring Experiment, J. Geophys. Res., 106, 14539–14550, doi:10.1029/2000JD900772, 2001.

Pinardi, G., Yu, H., Hendrick, F., Tack, F., Granville, J., Lambert, J.-C. and Van Roozendael, M.: End-to-end Validation of Total and Tropospheric NO_2 Columns from Atmospheric Composition Satellite Sensors, Atmospheric Composition Validation and Evolution, ESRIN, Italy, March 2013.

Platt, U. and Stutz, J.: Differential Optical Absorption Spec-troscopy. Springer-Verlag Heidelberg, Berlin, 229–375, 2008.

Richter, A., Burrows, J.P., Nüß, H., Granier, C. and Niemeier, U.: Increase in tropospheric nitrogen dioxide over China observed from space. Nature, 437(7055), pp.129-132, 2005

Richter, A., Wittrock, F. and Burrows, J.P.: SO_2 measurements with SCIAMACHY. In Proc. Atmospheric Science Conference (pp. 8-12). May, 2006

Richter, A., Wittrock, F., Schönhardt, A. and Burrows, J.P.: Quantifying volcanic SO_2 emissions using GOME2 measurements.Geophys. Res. Abstr., EGU2009-7679, EGU General Assembly, 2009.

Rix, M., Valks, P., Hao, N., Loyola, D. G., Schlager, H., Huntrieser, H. H., Flemming, J., Koehler, U., Schumann, U., and Inness, A.: Volcanic SO2, BrO and plume height estimations using GOME-2 satellite measurements during the eruption of Eyjafjallajökull in May 2010, J. Geophys. Res., 117, D00U19, doi:10.1029/2011JD016718, 2012.

Rozanov, A., Rozanov, V., Buchwitz, M., Kokhanovsky, A., and Burrows, J.: SCIATRAN 2.0 - A new radiative transfer model for geophysical applications in the 175-2400 nm spectral region, in: Atmospheric Remote Sensing: Earth's Surface, Troposphere, Stratosphere and Mesosphere - I, edited by Burrows, J. and Eichmann, K., vol. 36 of ADVANCES IN SPACE RESEARCH, 1015-1019, 2005.

Seinfeld, J. H. and Pandis, S. N.: Atmospheric Chemistry and Physics—From Air Pollution to Climate Change. John Wiley, New York, 1998.

Sens., 44, 1259–1266.

Shaiganfar, R., Beirle, S., Sharma, M., Chauhan, A., Singh, R. P., and Wagner, T.: Estimation of Nox emissions from Delhi using Car MAX-DOAS observations and comparison with OMI satellite data, Atmos. Chem. Phys., 11, 10871–10887, doi:10.5194/acp-11-10871-2011, 2011.

Spurr, R.J.D., Kurosu, T.P. and Chance, K.V.: A linearized discrete ordinate radiative transfer model for atmospheric remote-sensing retrieval. Journal of Quantitative Spectroscopy and Radiative Transfer, 68(6), pp.689-735, 2001

Spurr, R.: LIDORT and VLIDORT: Linearized pseudo-spherical scalar and vector discrete ordiate radiative transfer models for use in remote sensing retrieval problems, in Light Scattering Reviews 3 , edited by A. Kokhanovsky, pp. 229 – 275, Springer, Berlin, doi:10.1007/978-3-540-48546-9_7, 2008.

Stammes, P.: Errors in UV reflectivity and albedo calculations due to neglecting polarisation, SPIE 2311, 227-235, 1994.

Stammes, P., Sneep, M., de Haan, J. F., Veefkind, J. P., Wang, P. and Levelt, P. F.: Effective cloud fractions from the Ozone Moni-toring Instrument: Theoretical framework and validation, J. Geo-phys. Res., 113, D16S38, doi:10.1029/2007JD008820, 2008.

Stavrakou, T., Müller, J.-F., Boersma, K. F., van der A, R. J., Kurokawa, J., Ohara, T., and Zhang, Q.: Key chemical NOx sink uncertainties and how they influence top-down emissions of nitrogen oxides, Atmos. Chem. Phys., 13, 9057-9082, doi:10.5194/acp-13-9057-2013, 2013.

Stavrakou, T., Müller, J.-F., Bauwens, M., De Smedt, I., Van Roozendael, M., De Mazière, M., Vigouroux, C., Hendrick, F., George, M., Clerbaux, C., Coheur, P.-F., and Guenther, A.: How consistent are top-down hydrocarbon emissions based on

formaldehyde observations from GOME-2 and OMI?, Atmos. Chem. Phys., 15, 11861-11884, doi:10.5194/acp-15-11861-2015, 2015.

Theys, N., De Smedt, I., Gent, J., Danckaert, T., Wang, T., Hendrick, F., Stavrakou, T., Bauduin, S., Clarisse, L., Li, C., Krotkov, N., Yu, H., Brenot, H., and Van Roozendael, M.: Sulfur dioxide vertical column DOAS retrievals from the Ozone Monitoring Instrument: Global observations and comparison to ground - based and satellite data. Journal of Geophysical Research: Atmospheres, 120(6), 2470-2491, 2015.

Valks, P., Pinardi, G., Richter, A., Lambert, J.-C., Hao, N., Loyola, D., Van Roozendael, M., and Emmadi, S.: Operational total and tropospheric NO_2 column retrieval for GOME-2, Atmos. Meas. Tech., 4, 1491–1514,doi:10.5194/amt-4-1491-2011, 2011.

van der A, R. J., Eskes, H. J., Boersma, K. F., Van Noije, T. P. C., Van Roozendael, M., De Smedt, I., Peters, D.H.M.U. and Meijer, E.W., : Trends, seasonal variability and dominant NOx source derived from a ten year record of NO_2 measured from space. Journal of Geophysical Research: Atmospheres, 113(D4), 2008

Van Roozendael, M., Fayt, C., Post, P., Hermans, C., Lambert, J.-C.: Retrieval of BrO and NO2 from UV-Visible Observations, in: Sounding the troposphere from space: a new Era for Atmospheric Chemistry. The TROPOSAT Final Report. Peter Borrell, Patricia M. Borrell, John P. Burrows and Ulrich Platt (editors), Springer Verlag, 155-166, 2003

Veefkind, J.P., Aben, I., McMullan, K., Förster, H., De Vries, J., Otter, G., Claas, J., Eskes, H.J., De Haan, J.F., Kleipool, Q. and Van Weele, M.: TROPOMI on the ESA Sentinel-5 Precursor: A GMES mission for global observations of the atmospheric composition for climate, air quality and ozone layer applications. Remote Sensing of Environment, 120, pp.70-83, 2012.

Vlemmix, T., Piters, A. J. M., Stammes, P., Wang, P., and Levelt, P. F.: Retrieval of tropospheric NO_2 using the MAX-DOAS method combined with relative intensity measurements for aerosol correction, Atmos. Meas. Tech., 3, 1287–1305, 2010.

Vlemmix, T., Piters, A. J. M., Berkhout, A. J. C., Gast, L. F. L., Wang, P., and Levelt, P. F.: Ability of the MAX-DOAS method to derive profile information for NO2: can the boundary layer and free troposphere be separated?, Atmos. Meas. Tech., 4, 2659–2684, 2011.

Vlemmix, T., Eskes, H. J., Piters, A. J. M., Schaap, M., Sauter, F. J., Kelder, H., & Levelt, P. F.: MAX-DOAS tropospheric nitrogen dioxide column measurements compared with the Lotos-Euros air quality model, Atmospheric Chemistry and Physics, 15(3), 1313-1330, 2015a

Vlemmix, T., Hendrick, F., Pinardi, G., De Smedt, I., Fayt, C., Hermans, C., Piters, A., Wang, P., Levelt, P., and Van Roozendael, M.: MAX-DOAS observations of aerosols, formaldehyde and nitrogen dioxide in the Beijing area: comparison of two profile retrieval approaches, Atmos. Meas. Tech., 8, 941-963, doi:10.5194/amt-8-941-2015, 2015b.

Wagner, T., B. Dix, C. von Friedeburg, Frieß, U., Sanghavi, S., Sinreich, R. and Platt, U.: MAX-DOAS O_4 measurements: A new technique to derive information on atmospheric aerosols—Principles and information content, J. Geophys. Res., 109, D22205, 2004.

Wagner, T., Beirle, S., Brauers, T., Deutschmann, T., Frieß, U., Hak, C., Halla, J. D., Heue, K. P., Junkermann, W., Li, X., Platt, U. and Pundt-Gruber, I.: Inversion of tropospheric profiles of aerosol extinction and HCHO and NO_2 mixing ratios from MAX-DOAS observations in Milano during the summer of 2003 and comparison with independent data sets, Atmos. Meas. Tech. Discuss, 4, 3891–3964, 2011.

Wagner, T., Apituley, A., Beirle, S., Dörner, S., Friess, U., Rem-mers, J., and Shaiganfar, R.: Cloud detection and classification based on MAX-DOAS observations, Atmos. Meas. Tech., 7, 1289–1320, doi:10.5194/amt-7-1289-2014, 2014.

Wang, P., Stammes, P., van der A, R., Pinardi, G. and van Roozendael, M.: FRESCO+: an improved O2 A-band cloud retrieval algorithm for tropospheric trace gas retrievals, Atmos. Chem. Phys., 8, 6565–6576, 2008.

Wang, Y., Li, A., Xie, P. H., Chen, H., Xu, J., Wu, F. C., G., L. J., and Q., L. W.: Retrieving vertical profile of aerosol extinction by multi-axis differential optical absorption spectroscopy, Acta Phys. Sin., 16, doi: 10.7498/aps.62.180705, http://wulixb.iphy.ac.cn/EN/abstract/abstract54703.shtml#, 2013a.

Wang, Y., Li, A., Xie, P. H., Chen, H., Mou, F. S., Xu, J., Wu, F. C., Zeng, Y., Liu, J. G. and Liu, W. Q.: Measuring tropospheric vertical distribution and vertical column density of NO2 by multi-axis differential optical absorption spectroscopy, Acta Phys. Sin., 16, DOI:10.7498/aps.62.200705, http://wulixb.iphy.ac.cn/EN/abstract/abstract56201.shtml, 2013b.

Wang, Y., Penning de Vries, M., Xie, P. H., Beirle, S., Dörner, S., Remmers, J., Li, A., and Wagner, T.: Cloud and aerosol classification for 2.5 years of MAX-DOAS observations in Wuxi (China) and comparison to independent data sets, Atmos. Meas. Tech., 8, 5133-5156, doi:10.5194/amt-8-5133-2015, 2015.

Wang, Y., Lampel, J., Xie, P., Beirle, S., Li, A., Wu, D., and Wagner, T.: Ground-based MAX-DOAS observations of tropospheric aerosols, NO_2, SO_2 and HCHO in Wuxi, China, from 2011 to 2014, Atmos. Chem. Phys. Discuss., doi:10.5194/acp-2016-282, in review, 2016.

Williams, J. E., Scheele, M. P., van Velthoven, P. F. J., Cammas, J.-P., Thouret, V., Galy-Lacaux, C., and Volz-Thomas, A.: The influence of biogenic emissions from Africa on tropical tropospheric ozone during 2006: a global modelling study, Atmos. Chem. Phys., 9, 5729–5749, doi:10.5194/acp-9-5729-2009, 2009

Wittrock, F., Oetjen, H., Richter, A., Fietkau, S., Medeke, T., Rozanov, A., and Burrows, J. P.: MAX-DOAS measurements of atmospheric trace gases in Ny-Alesund – Radiative transfer studies and their application, Atmos. Chem. Phys., 4, 955–966, 2004.

Wittrock, F., Richter, A., Oetjen, H., Burrows, J. P., Kanakidou, M., Myriokefalitakis, S., Volkamer, R., Beirle, S., Platt, U., and Wagner, T.: Simultaneous global observations of glyoxal and formaldehyde from space, Geophys. Res. Lett., 33, L16804, doi:10.1029/2006GL026310, 2006a.

Wittrock, F.: The Retrieval of Oxygenated Volatile Organic Compounds by Remote Sensing Techniques. Ph.D., University of Bremen, Bremen, Germany, 2006b, Available at: http://www.doas-bremen.de/paper/diss_wittrock_06.pdf (last accessed Dec 2015).

Xue, L., Ding, A., Gao, J., Wang, T., Wang, W., Wang, X., Lei, H., Jin, D., and Qi, Y.: Aircraft measurements of the vertical distribution of sulfur dioxide and aerosol scattering coefficient in China. Atmospheric Environment, 44(2), 278-282, 2010.

Yang, K., Krotkov, N.A., Krueger, A.J., Carn, S.A., Bhartia, P.K. and Levelt, P.F.: Retrieval of large volcanic SO2 columns from the Aura Ozone Monitoring Instrument: Comparison and limitations. Journal of Geophysical Research: Atmospheres, 112(D24), 2007

Yilmaz, S.: Retrieval of Atmospheric Aerosol and Trace Gas Vertical Profiles using Multi-Axis Differential Optical Absorption Spectroscopy, Dissertation submitted to the Combined Faculties for the Natural Sciences and for Mathematics of the Ruperto-Carola University of Heidelberg, Germany for the degree of Doctor of Natural Sciences, 2012.

Figures & Tables

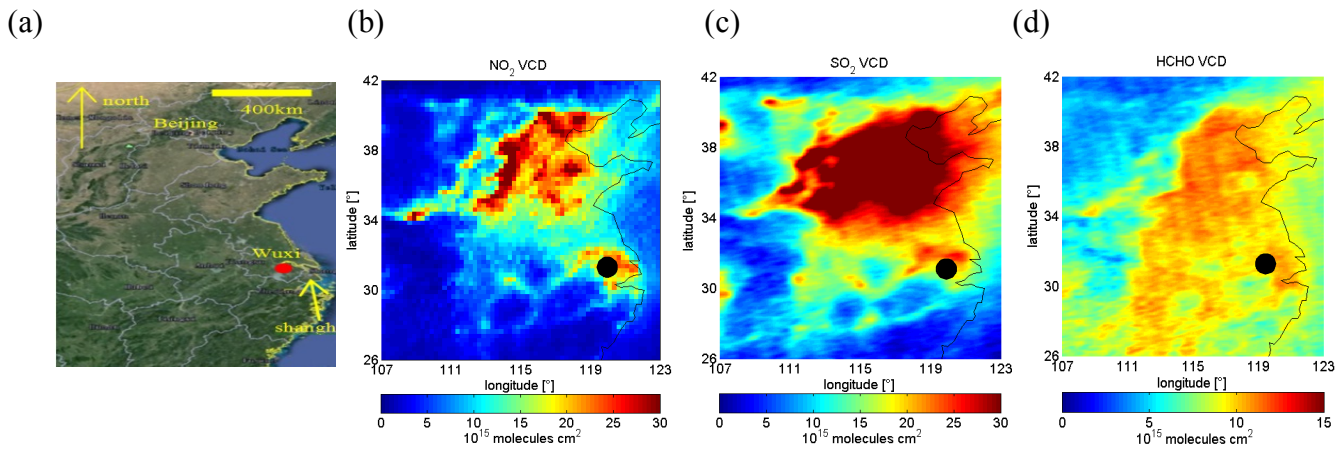

Figure 1: Wuxi city, in which the MAX-DOAS instrument is operated, is marked by the red dot in subfigure (a). Subfigures (b), (c) and (d) show maps of the averaged tropospheric VCDs of NO_2 from DOMINO 2, SO_2 and HCHO from BIRA derived from OMI observations over eastern China in the period from 2011 to 2014, respectively. The black dots indicate the location of Wuxi.

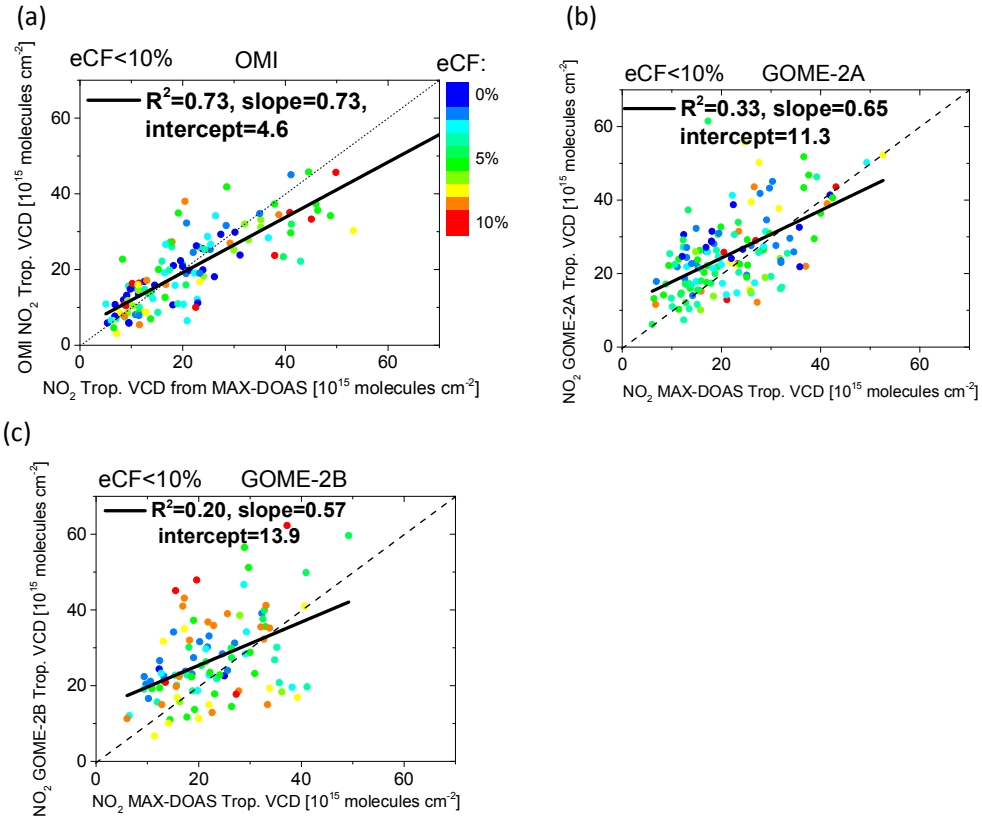

Figure 2: Daily average NO_2 tropospheric VCDs derived from OMI (a), GOME-2A (b) and GOME-2B (c) compared with the corresponding MAX-DOAS data for eCF<10%. The colors indicate the eCF.

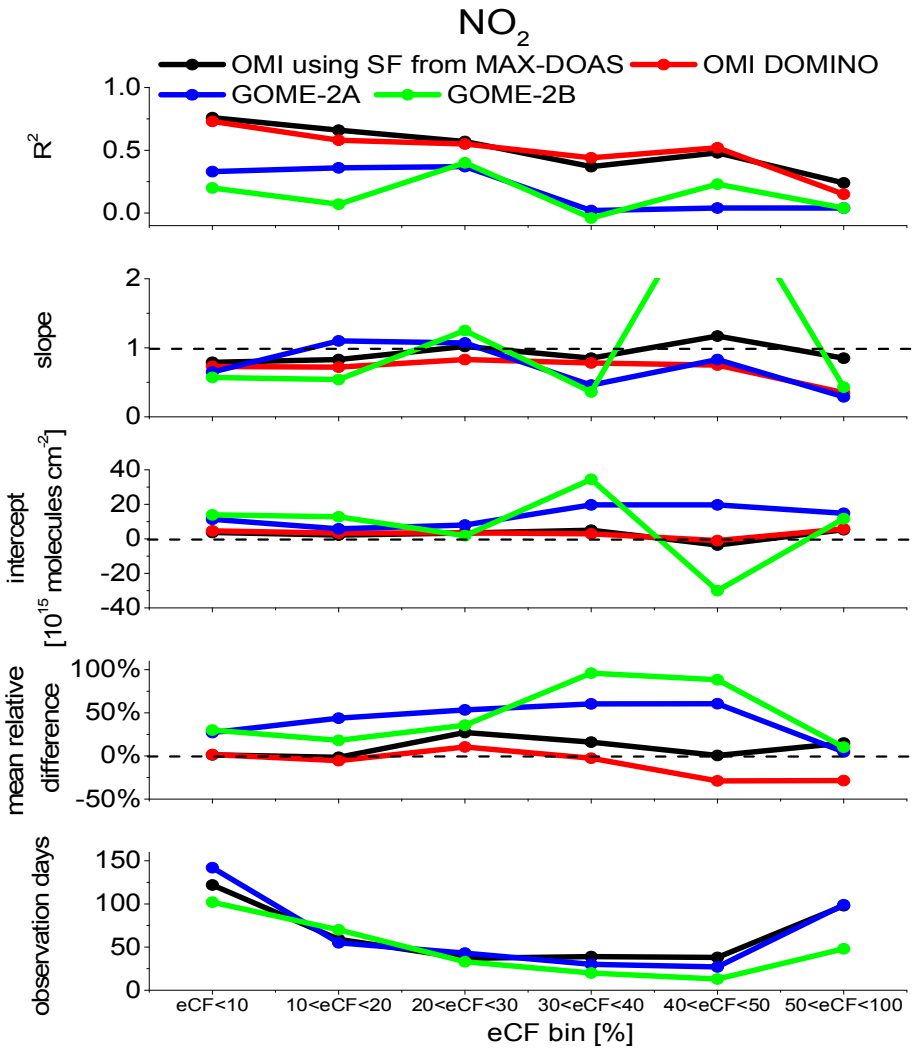

Figure 3: R^2, slopes, intercepts, mean relative differences (and the number of available days) derived from the comparisons of the NO_2 VCDs from different satellite instruments to the MAX-DOAS results for the different eCF bins. Note that the black and red curves represent the improved OMI VCDs with the a-priori shape factors derived from Wuxi MAX-DOAS observations (see section 3.2) and for the DOMINO 2 product, respectively.

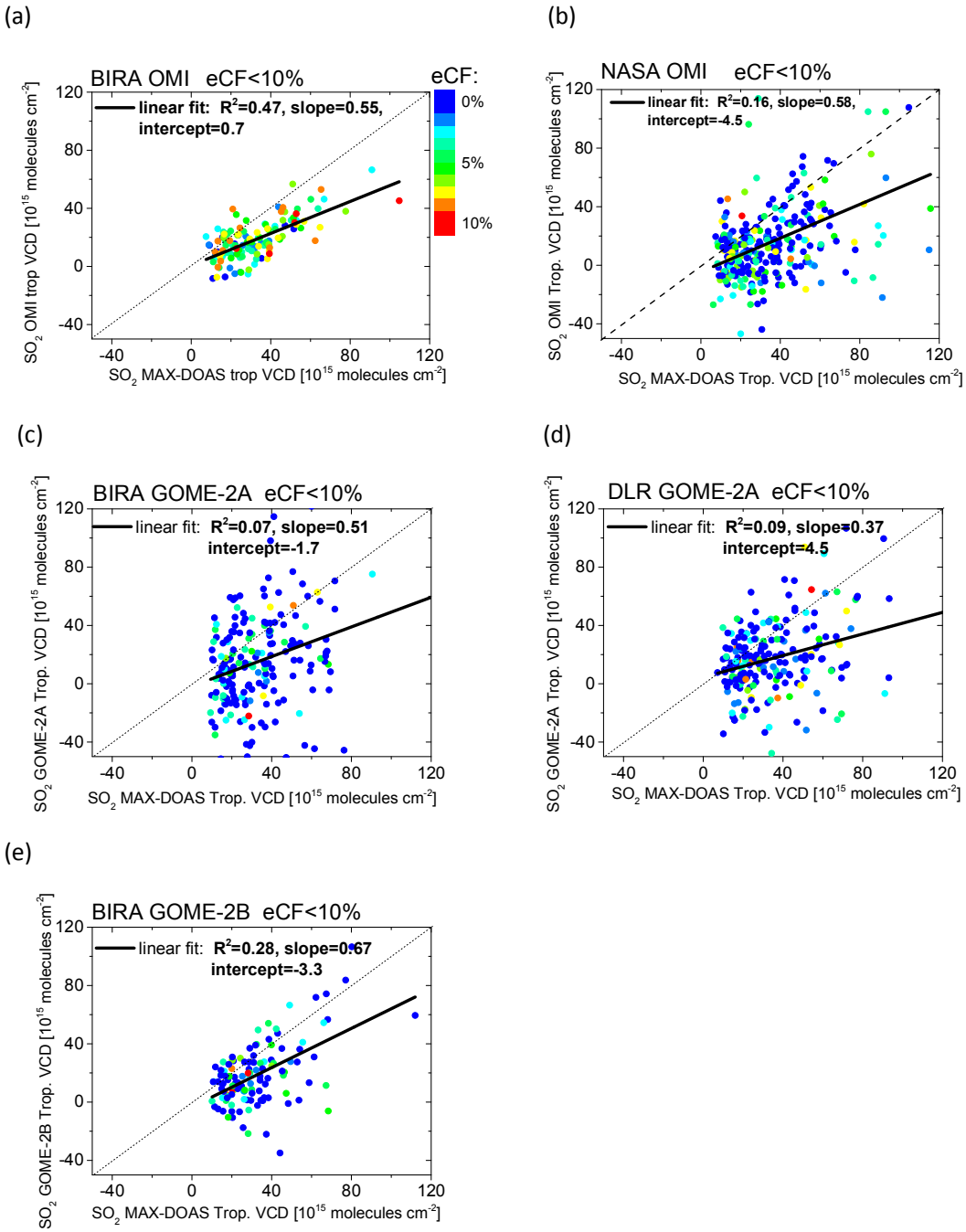

Figure 4: Daily averaged OMI SO_2 tropospheric VCDs from BIRA (a) and NASA (b), GOME -2A SO_2 tropospheric VCDs from BIRA (c) and DLR (d) and GOME-2B SO_2 tropospheric VCDs from BIRA (e) for eCF < 10% plotted versus the coincident MAX-DOAS results. The colors indicate the eCF.

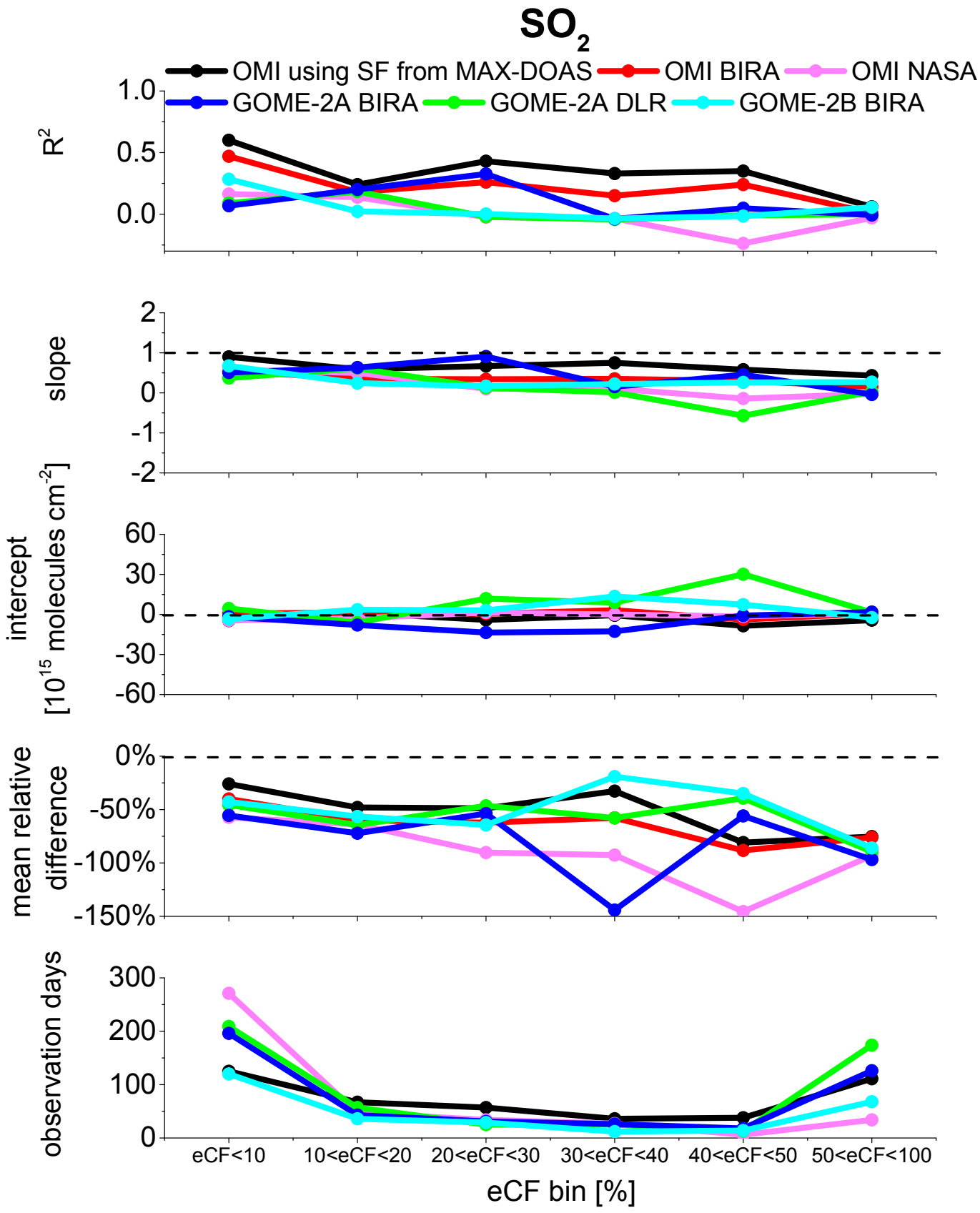

Figure 5: Same as Fig. 3 but for SO_2.

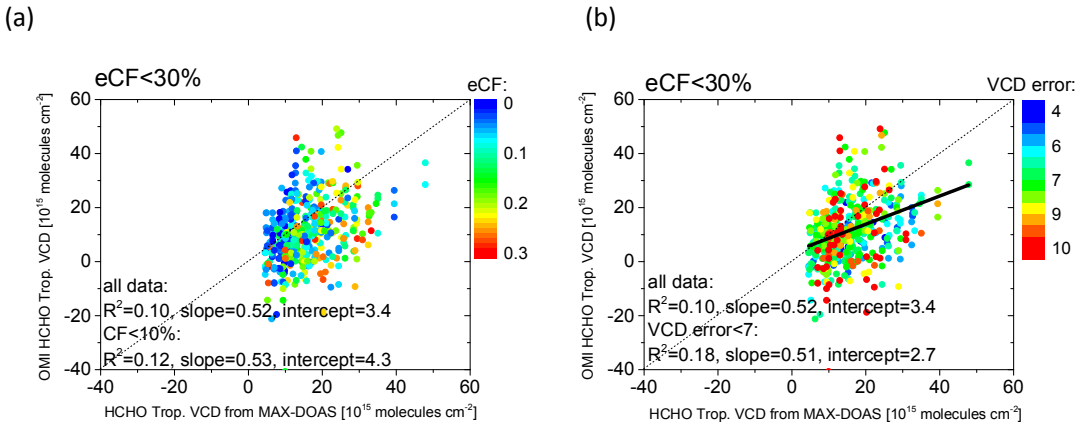

Figure 6: (a) HCHO tropospheric VCDs for OMI pixels for eCF<30% are plotted against those derived from MAX-DOAS observations with the color map of eCF; the linear regression parameters are acquired for eCF<30% and for eCF<10%, respectively. (b) Scattered plots are same as in (a), but with the color map of VCD fit error; linear regression parameters are acquired for all data and for VCD fit error <7×10^{15} molecules cm^{-2}.

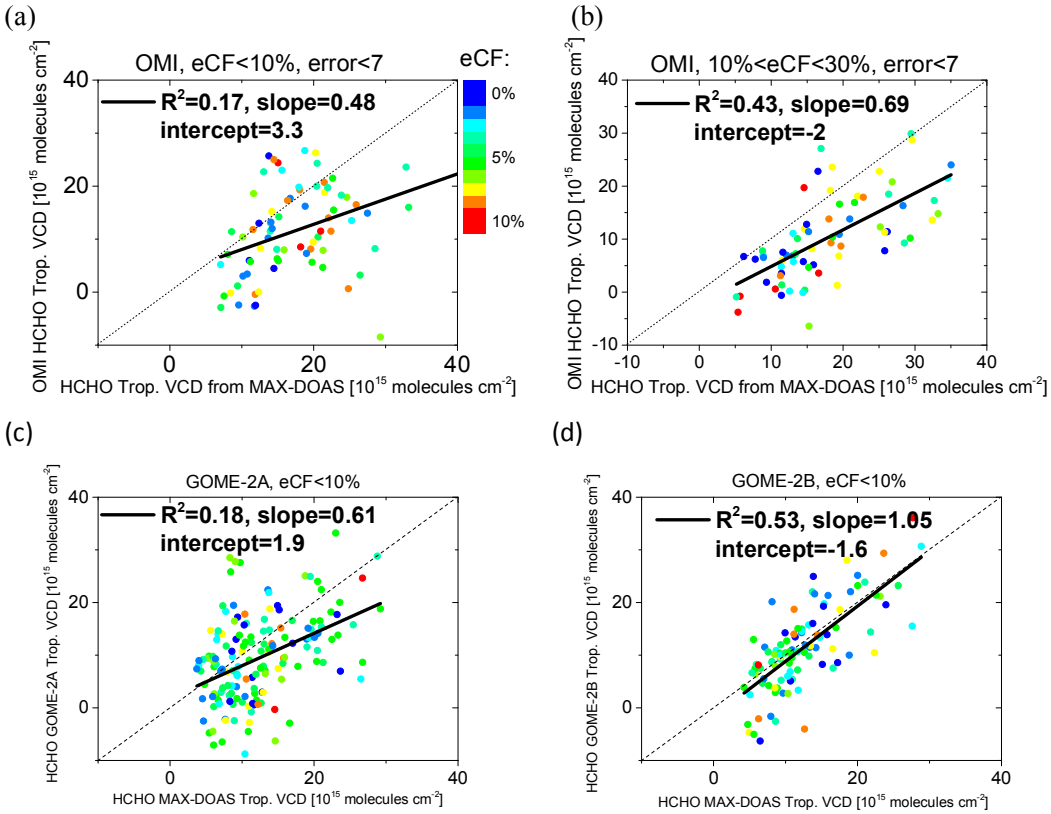

Figure 7: Same as Fig.2, but for HCHO.

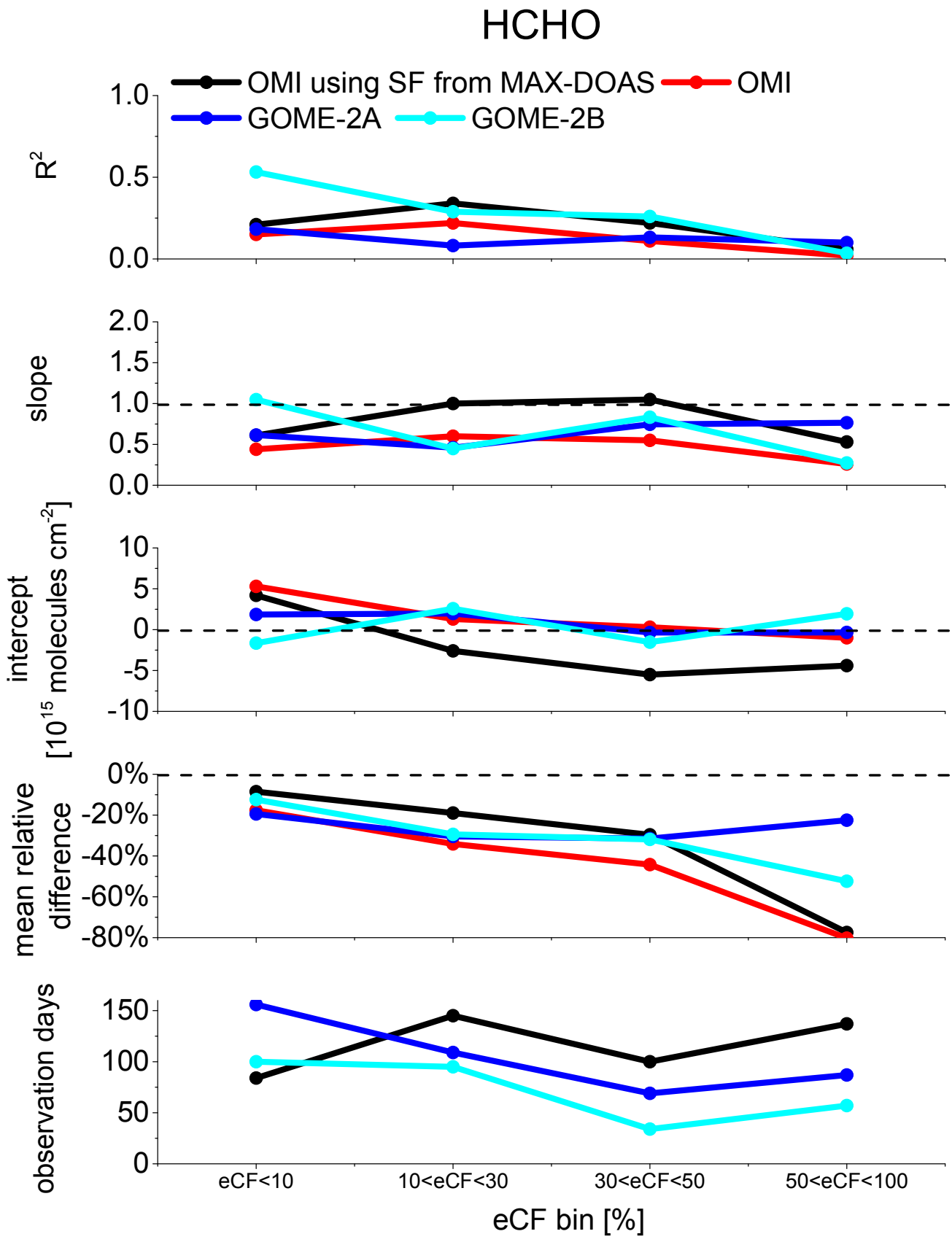

Figure 8: Same as Fig. 3 but for HCHO.

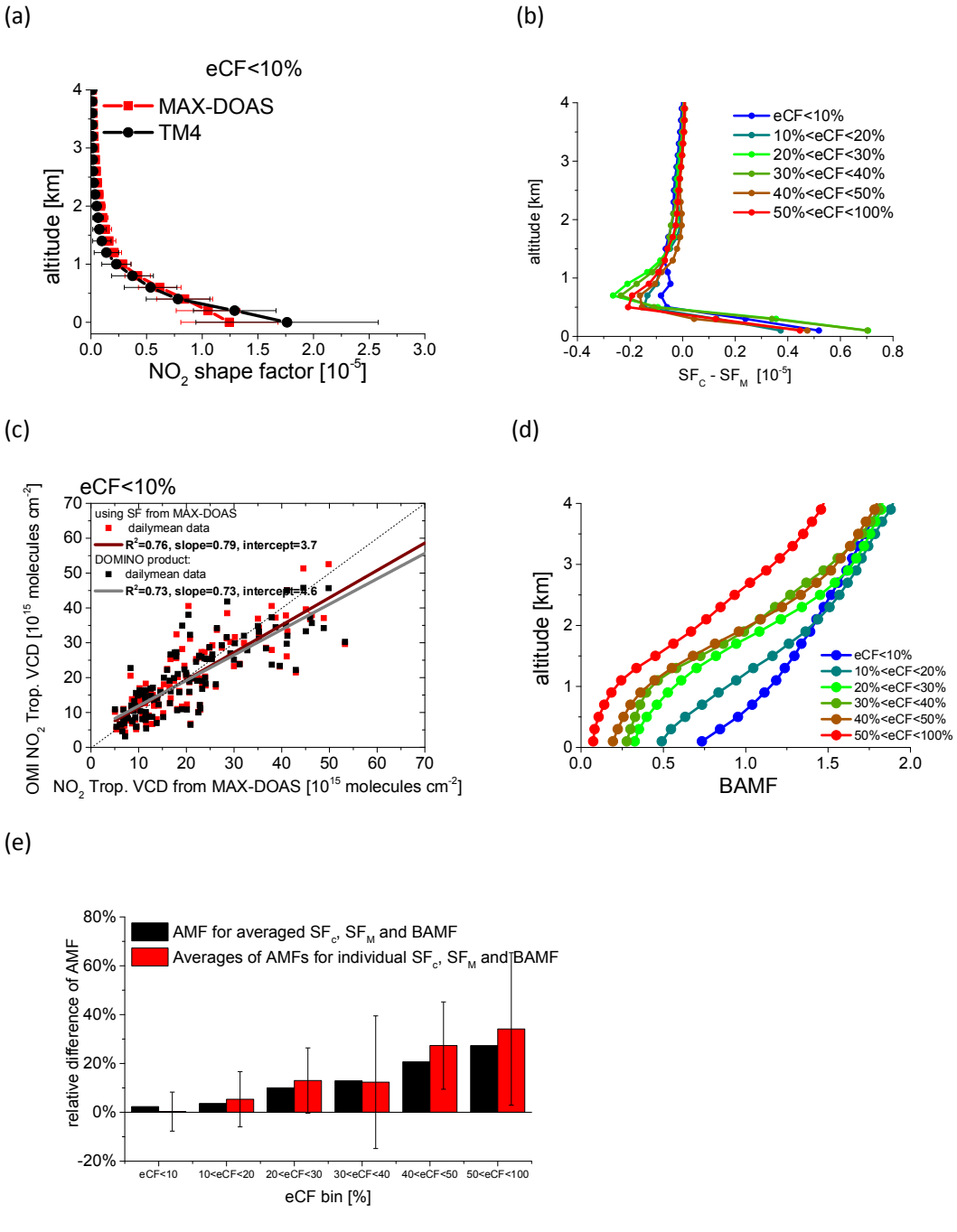

Figure 9: (a) Average NO_2 SFs and standard deviations derived from the MAX-DOAS observations and from the TM4 CTM (for the DOMINO product) for eCF < 10%. (b) Averaged differences between the NO_2 SFs from CTM (SF_C) and from MAX-DOAS (SF_M) for different eCF bins. (c) Daily averages of the original DOMINO NO_2 product and modified NO_2 product (based on MAX-DOAS SF) plotted against those from MAX-DOAS for eCF < 10%. (d) Averaged BAMF for satellite observation for different eCF bins. (e) Relative difference (RD) of satellite AMF using SF_C (AMF_{CTM}) or SF_M ($AMF_{MAX\text{-}DOAS}$) for different eCF bins. The error bars indicate the standard deviation of the RDs for each eCF bin. Black columns denote the RDs derived from the averaged SF_C, SF_M and BAMF (shown in subfigure (b) and (d)); red columns denote the averaged RDs for individual SF_C , SF_M and BAMF of each satellite observation.

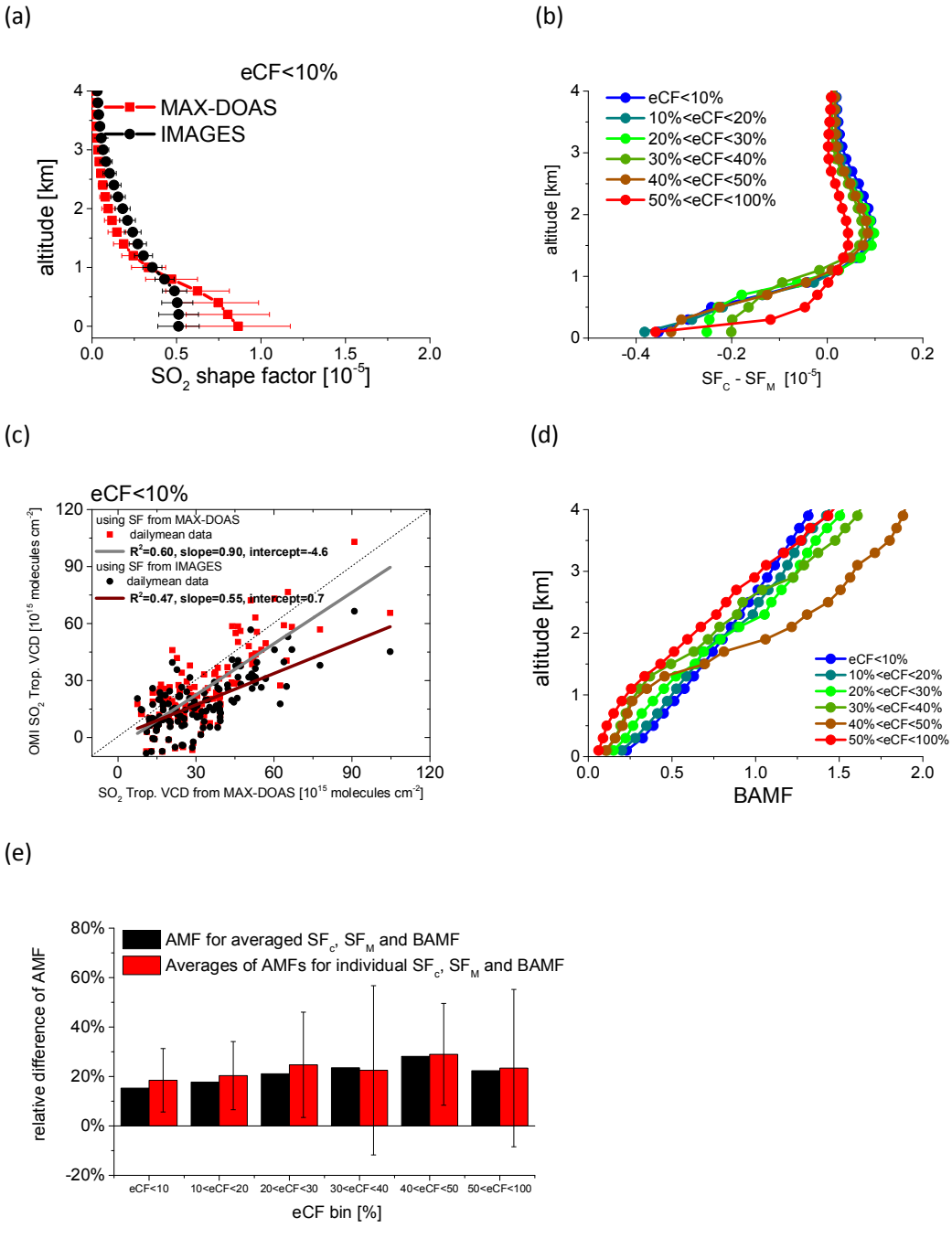

Figure 10: Similar as Fig. 9 but for the OMI BIRA SO_2 product. Note that the SF for the OMI BIRA product is obtained from the IMAGES CTM.

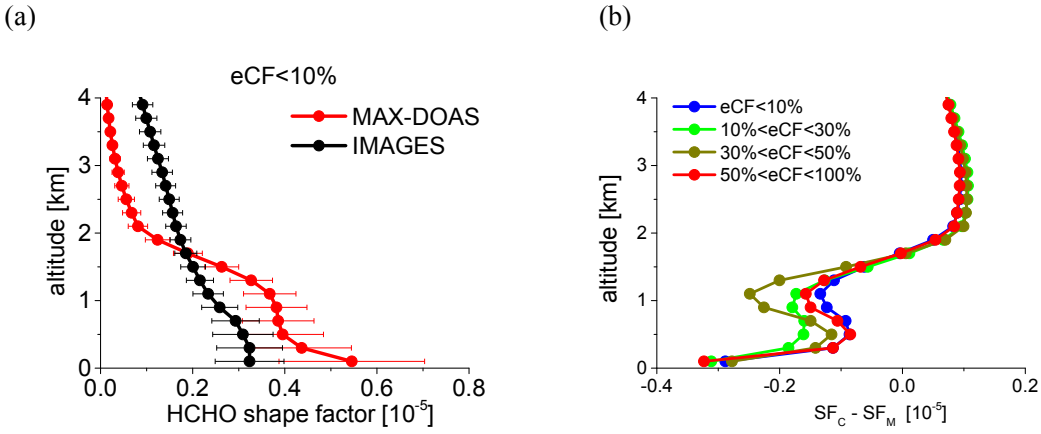

(c)

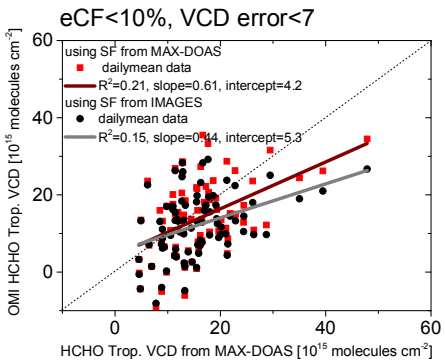

(d)

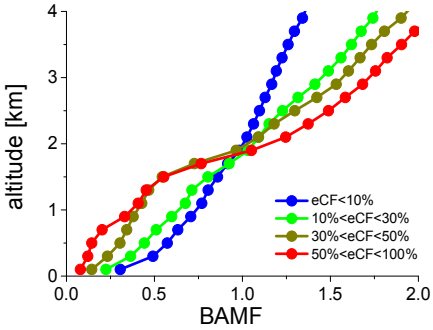

(e)

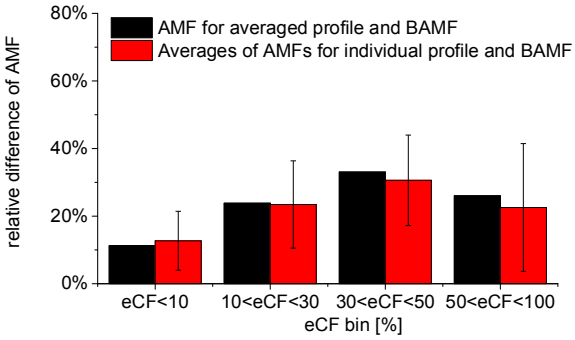

Figure 11: Same as Fig. 9 but for the OMI BIRA HCHO product and eCF bins of 0-10%, 10%-30%, 30% -50% and 50% -100%. Note that the SF for the OMI BIRA product is obtained from the IMAGES CTM.

(a)

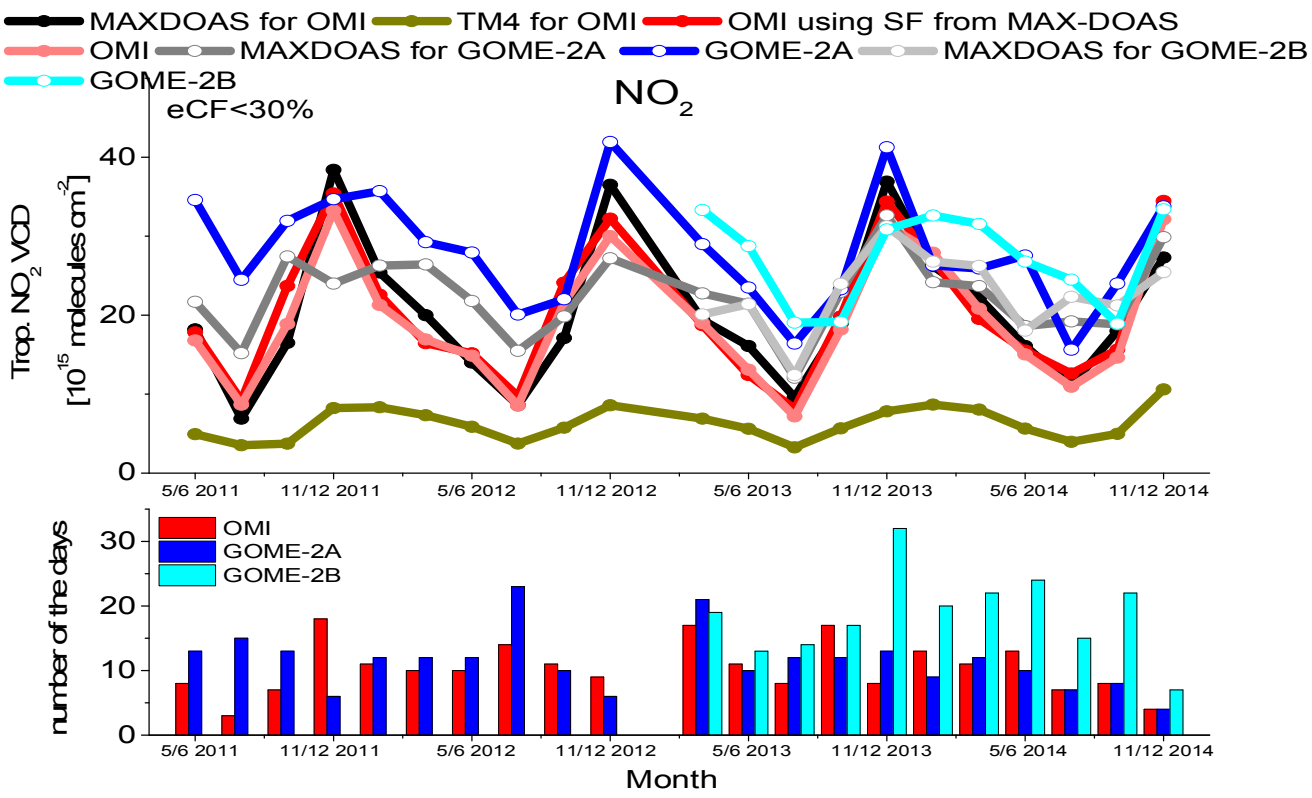

(b)

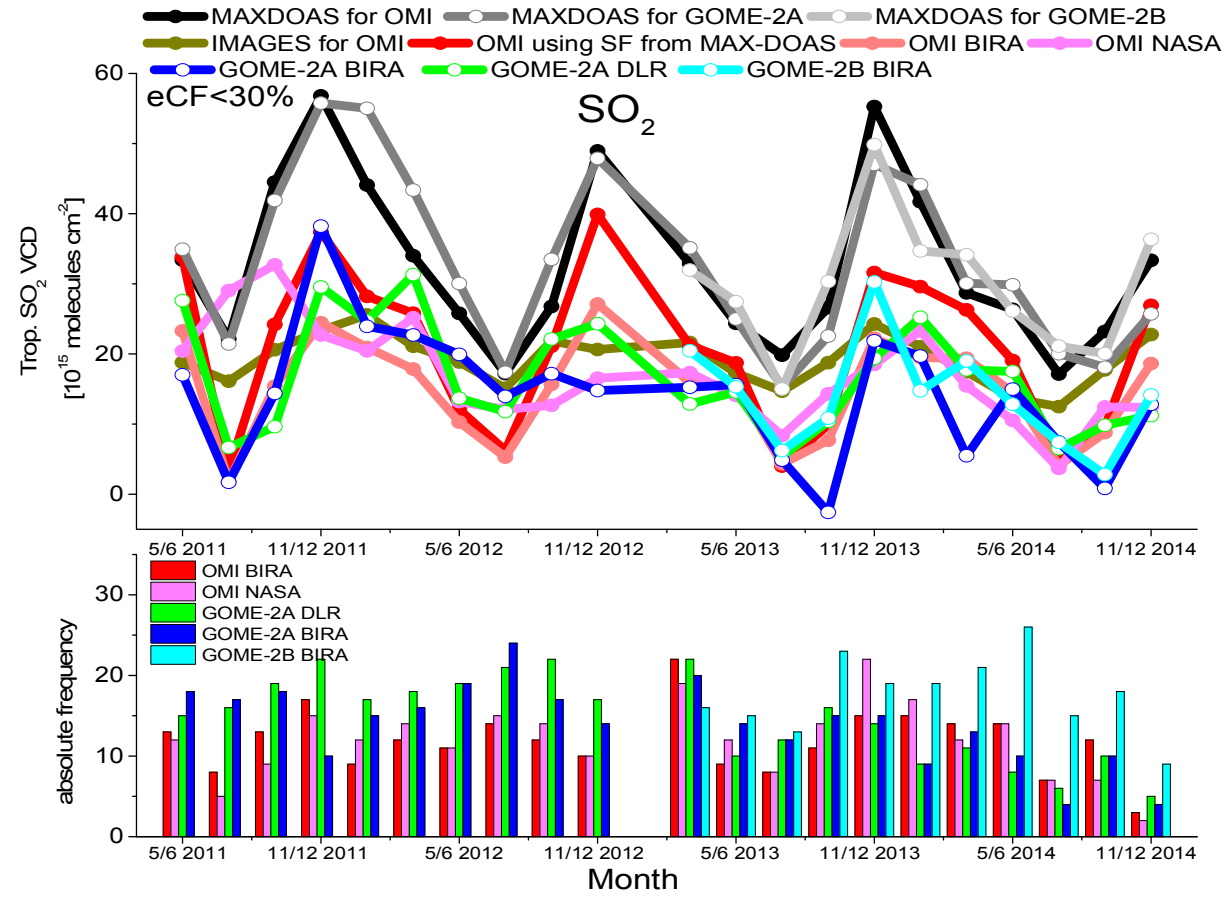

(c)

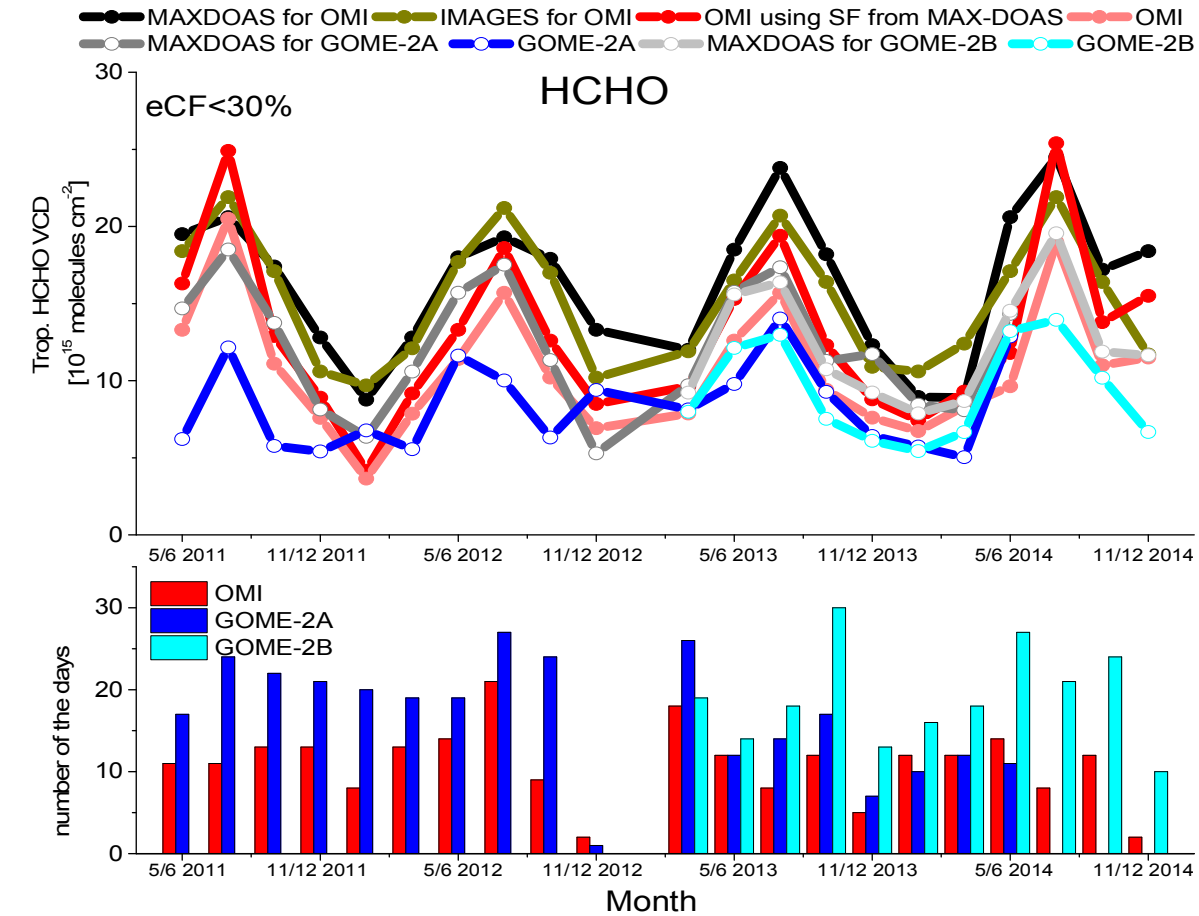

Figure 12: Bi-monthly averaged tropospheric VCDs of NO_2 (a), SO_2 (b), and HCHO (c) derived from coincident satellite and MAX-DOAS observations for eCF <30%. Also shown are the corresponding CTM results (TM4 for NO_2, IMAGES for SO_2 and HCHO). In all subfigures

the red and light red lines indicate the improved OMI tropospheric VCDs using the SFs from MAX-DOAS and the VCDs from the original OMI products, respectively. The numbers of the available days are shown in the bottom panel of each subfigure.

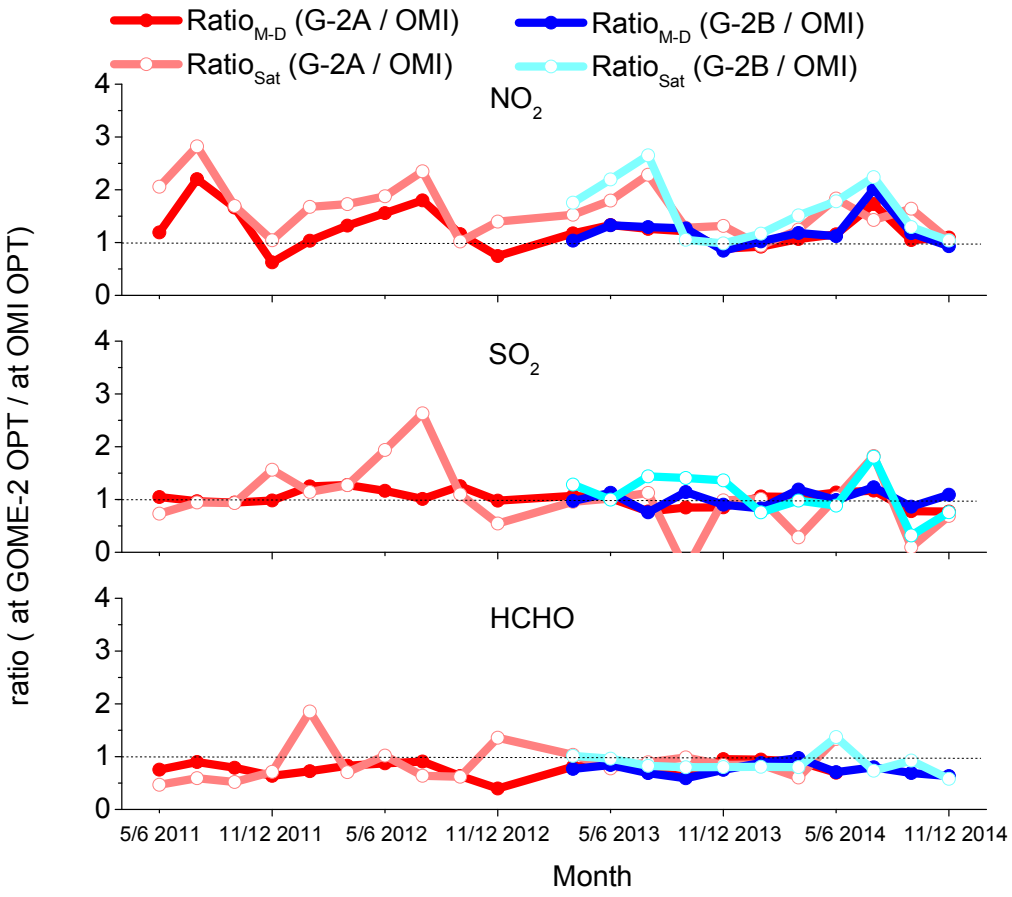

Figure 13: Ratios between the bi-monthly mean tropospheric VCDs from GOME-2A\B and OMI ($Ratio_{Sat}$) as well as the ratios between the corresponding MAX-DOAS observations ($Ratio_{M-D}$) for NO_2 (a), SO_2 (b), and HCHO (c), respectively. The light red (dark red) and light blue (dark blue) curves are corresponding to GOME-2A and GOME-2B results (coincident MAX-DOAS results with GOME-2A and GOME-2B), respectively. Note that for SO_2 the OMI and GOME-2A data from BIRA are used for the ratio calculations. The mean ratios for the shown data sets are presented in Table 1.

(a)

eCF<10% eCF<10% and CP>900hPa eCF<10%, CP>900hPa, VCD> threshold

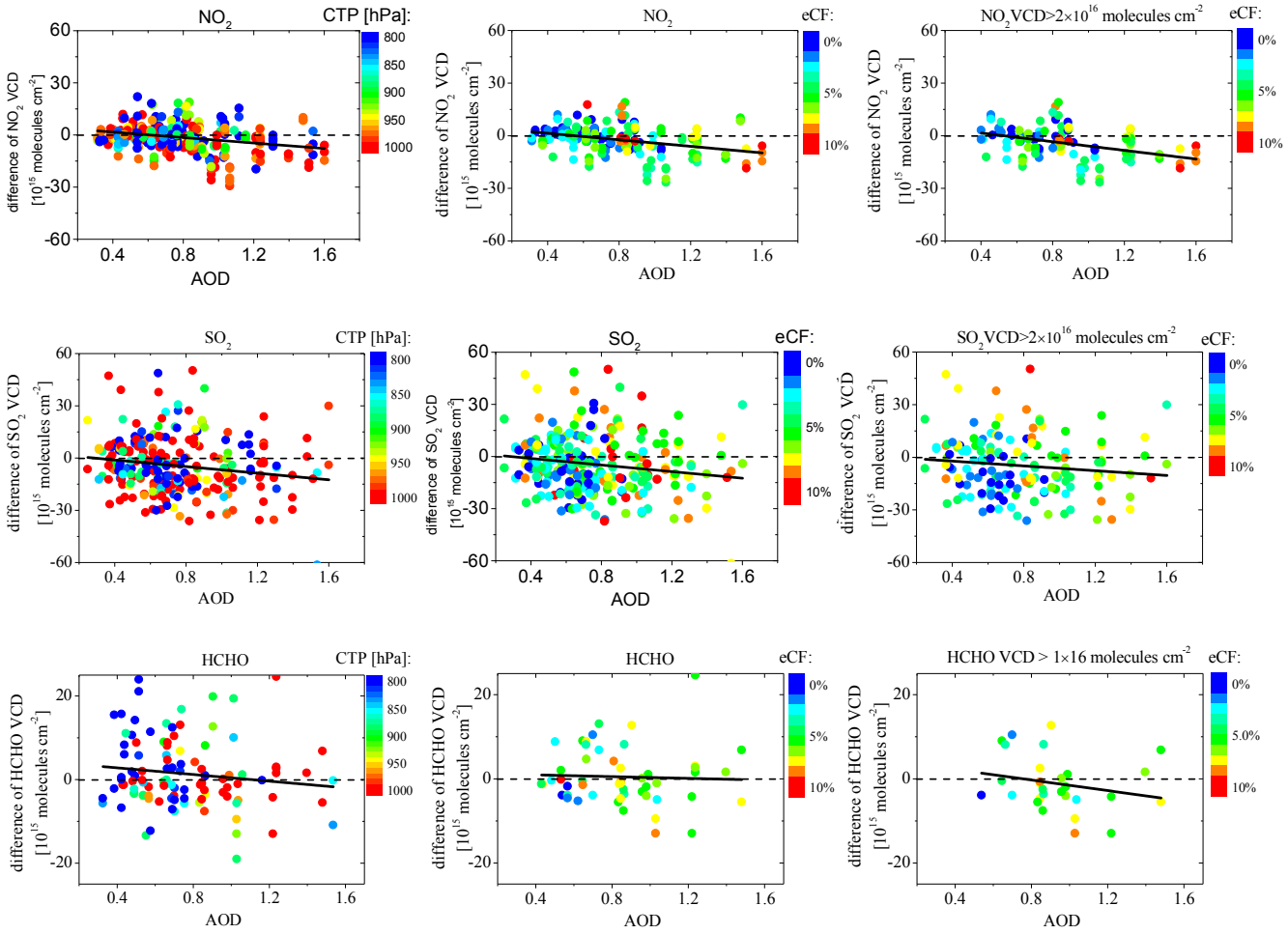

(b)

eCF<10% eCF<10% and CP>900hPa eCF<10%, CP>900hPa, VCD> threshold

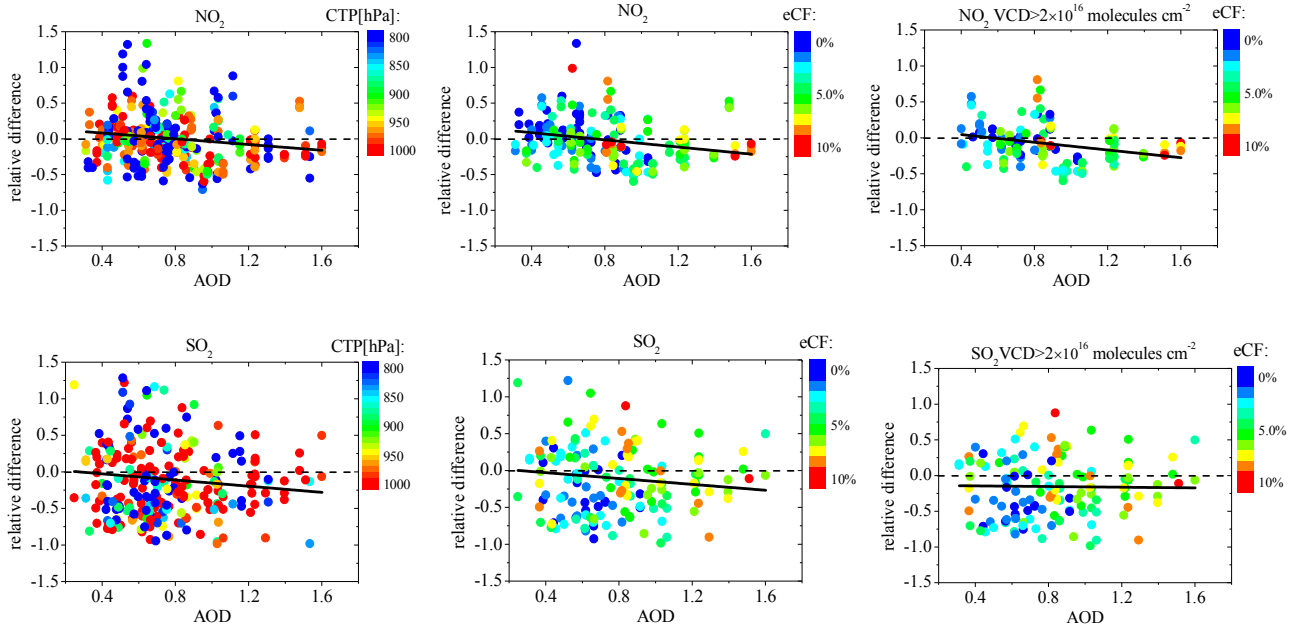

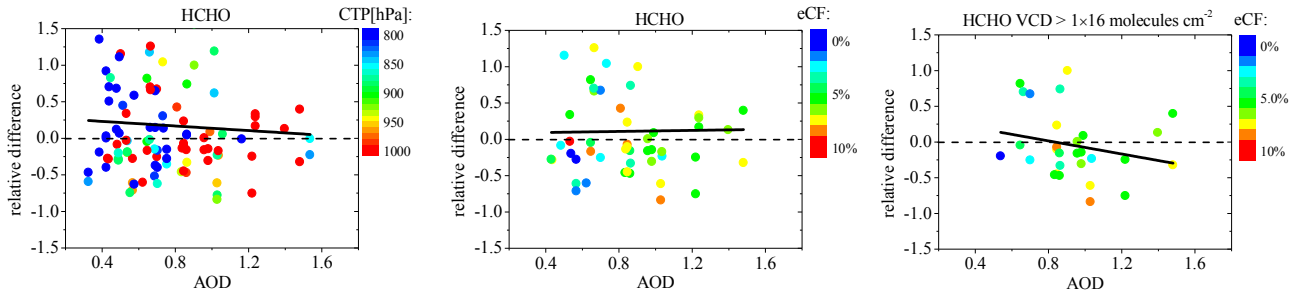

Figure 14: absolute differences (a) and relative differences (b) of tropospheric VCDs of NO_2, SO_2 and HCHO between individual OMI observations and MAX-DOAS observations plotted against the AODs derived from the MAX-DOAS observations. The data are differently screened in the left, center and right panels: eCF < 10% for the left; eCF <10% and CTP > 900hPa for the center; and eCF < 10%, CTP > 900hPa, and VCD > a specific threshold for the right (see text). Note that the OMI VCDs are the modified values using SFs derived from MAX-DOAS observations.

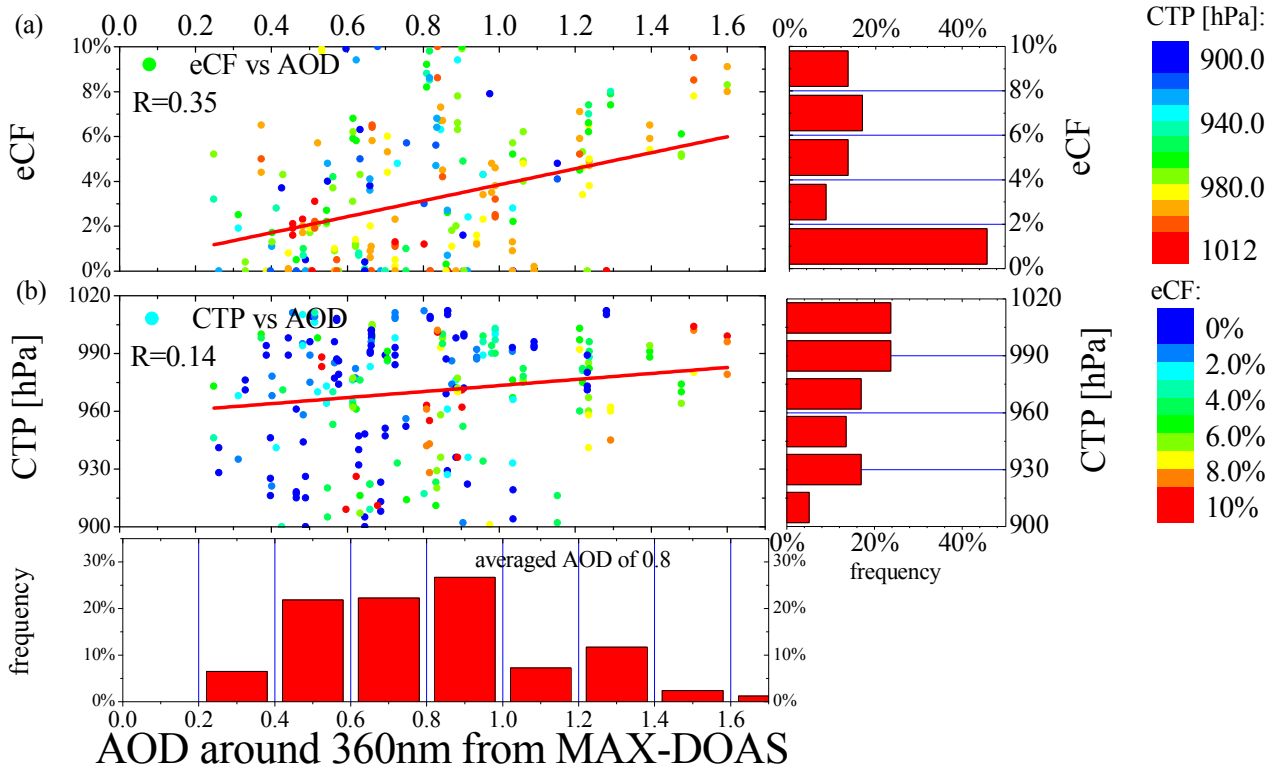

Figure 15: eCF and CTP from the OMI cloud algorithm for individual OMI observations are plotted against AOD at 360nm derived from MAX-DOAS observation (for eCF<10% and CTP > 900hPa). The red bars on the right and bottom indicate the frequency of eCF, CTP, and AOD in different value intervals. The red lines are the linear regressions of the scatter plots. The correlation coefficients are shown in the figure. The color of the dots in (a) and (b) indicates CTP and eCF, respectively.

(a)

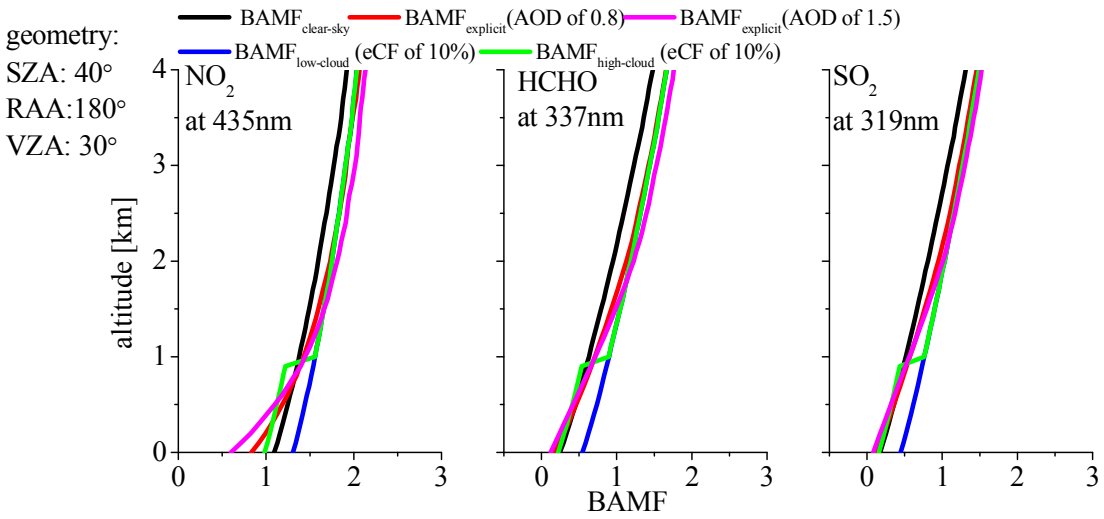

(b)

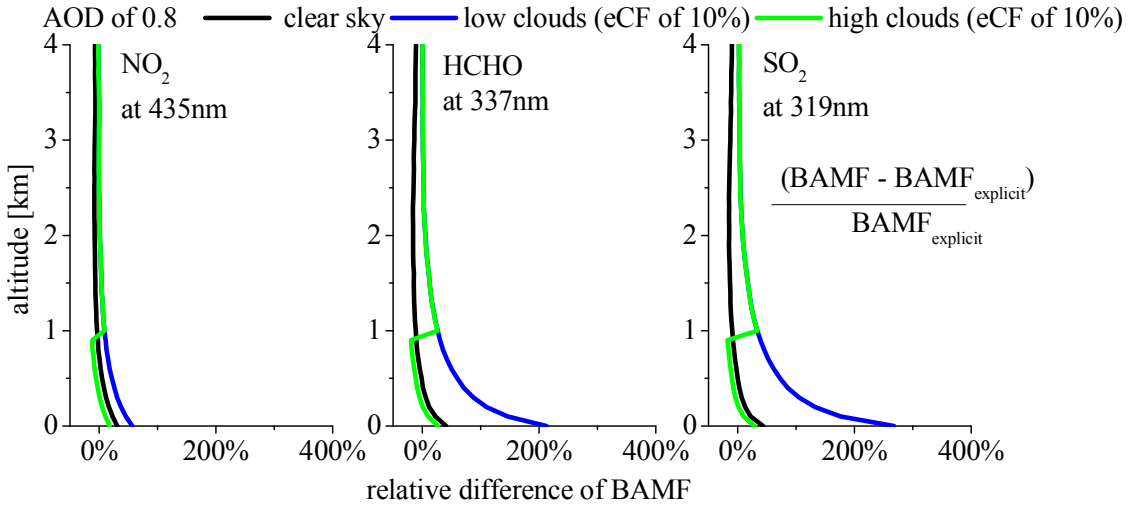

(c)

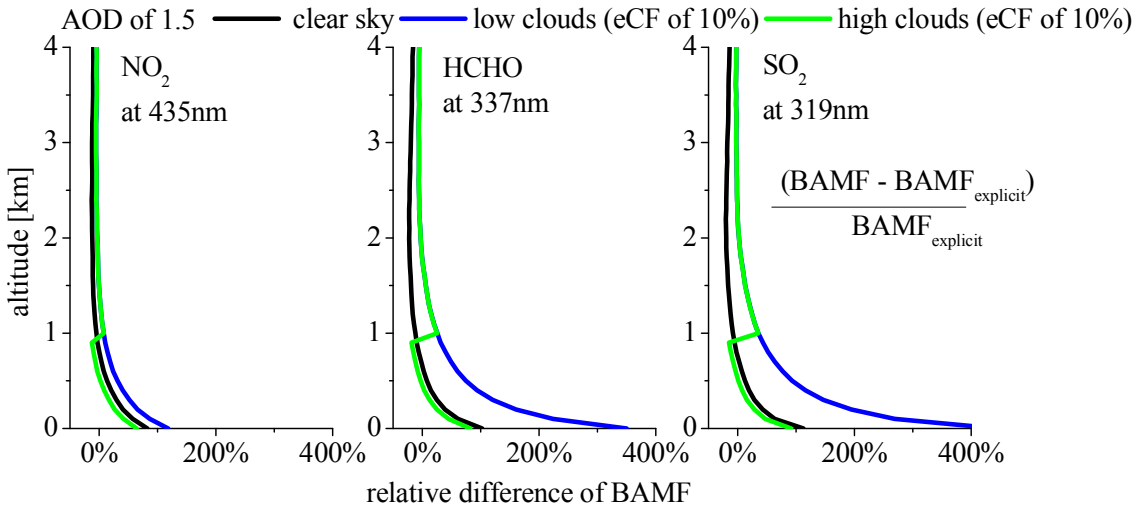

Figure 16: (a) simulated $BAMF_{clear-sky}$, $BAMF_{explicit}$ for AOD of 0.8 and 1.5, $BAMF_{low-cloud}$ (cloud at surface) and $BAMF_{high-cloud}$ (cloud at 1km) of NO_2 at 435nm, HCHO at 337nm and SO_2 at 319nm for one typical satellite observation (SZA of 40°, RAA of 180° and VZA of 30°). An effective cloud fraction of 10% is used in the calculations. (b) Relative differences of $BAMF_{clear-sky}$, $BAMF_{low\ clouds}$ and $BAMF_{high-clouds}$ compared to $BAMF_{explicit}$ for AOD of 0.8. (c) Same with (b) but $BAMF_{explicit}$ for AOD of 1.5.

(a)

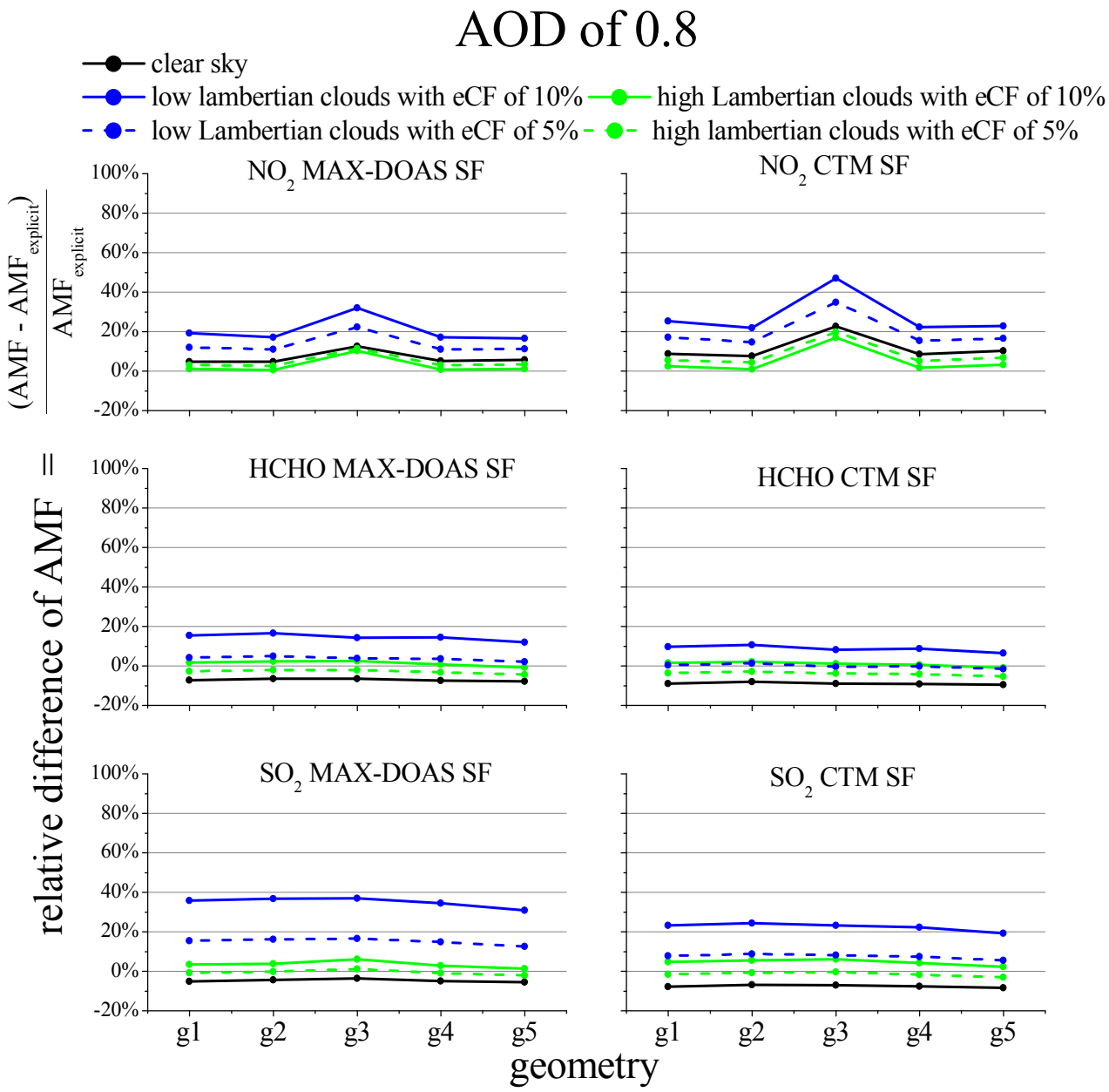
AOD of 0.8
clear sky
low lambertian clouds with eCF of 10%
high Lambertian clouds with eCF of 10%
low Lambertian clouds with eCF of 5%
high lambertian clouds with eCF of 5%
NO2 MAX-DOAS SF
NO2 CTM SF
HCHO MAX-DOAS SF
HCHO CTM SF
SO2 MAX-DOAS SF
SO2 CTM SF
100%
80%
60%
40%
20%
0%
-20%
g1
g2
g3
g4
g5
geometry
relative difference of AMF = (AMF - AMF explicit) / AMF explicit

(b)

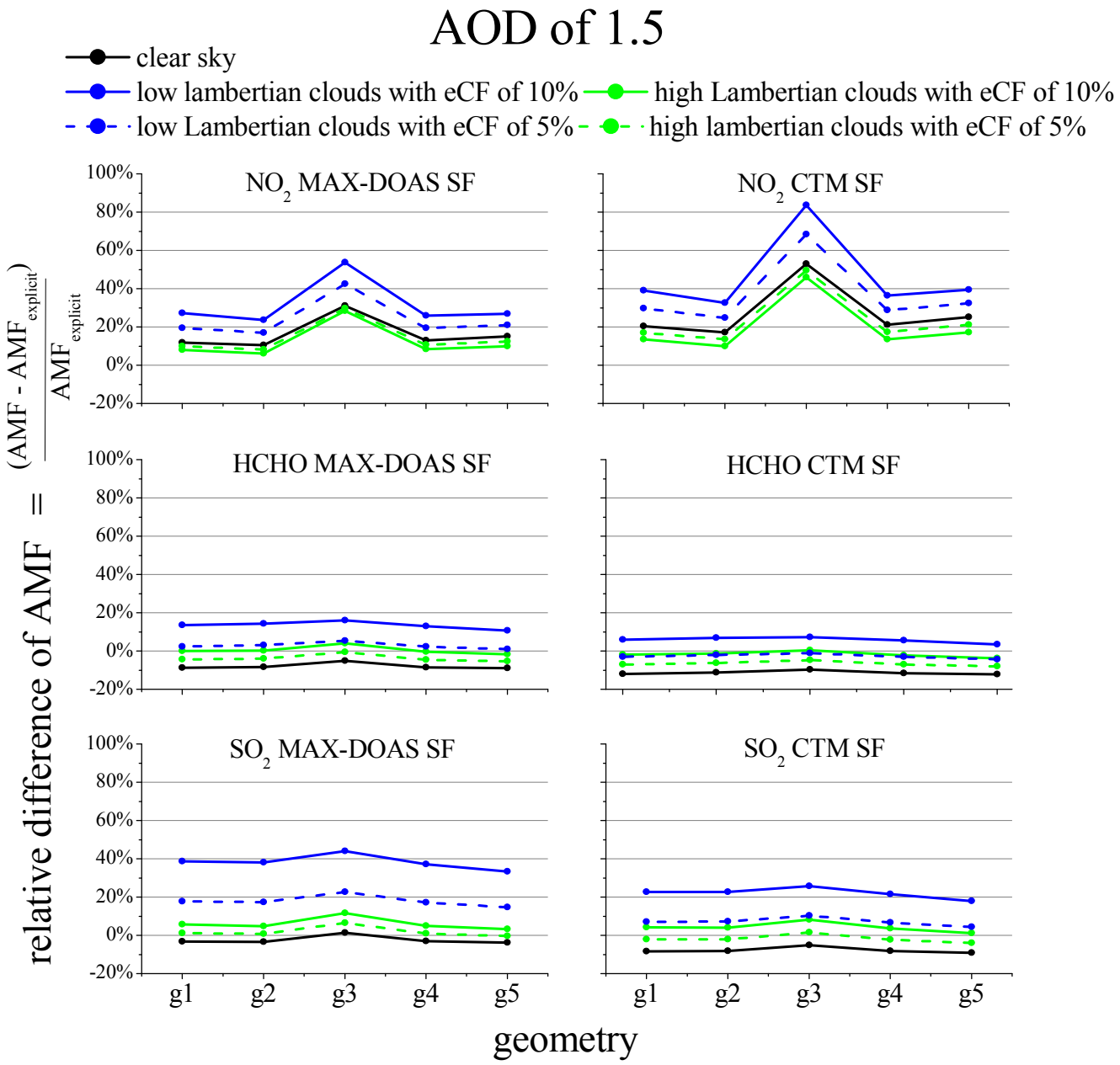

Figure 17: Relative differences between AMFs calculated for different cloud assumptions (for detail see text) and AMFs for explicit aerosol profiles for three trace gases. The labels at the x-axis indicate five different observation geometries (see Table 2). The MAX-DOAS and CTM SFs are used for the calculations shown in the left and right column. Explicit aerosol profiles of AOD of 0.8 and 1.5 are used in subfigure (a) and (b), respectively.

Table 1 Mean ratios for the data presented in Fig. 13.

	$Ratio_{M-D}$ (G-2A / OMI)	$Ratio_{Sat}$ (G-2A / OMI)	$Ratio_{M-D}$ (G-2B / OMI)	$Ratio_{Sat}$ (G-2B / OMI)
NO_2	1.25	1.62	1.20	1.61
SO_2	1.02	1.02	1.01	1.09
HCHO	0.78	0.88	0.76	0.87

Table 2 Observation geometry scenarios for BAMF and AMF calculations with different aerosol and cloud assumptions.

Scenario	Solar zenith angle [°]	View zenith angle[°]	Relative azimuth angle[°]
g1	40	30	180
g2	10	30	180
g3	70	30	180
g4	40	0	180
g5	40	30	0